

AD-A092 942

UTAH STATE UNIV LOGAN

F/G 7/4

THERMOSPHERIC DIAGNOSTICS USING IN SITU PROBING BY ELECTRON-BEAM--ETC(U)

JAN 80 W R PENDLETON, L C HOWLETT

F19628-78-C-0103

NI

UNCLASSIFIED

AFGL-TR-80-0047

40  
A27-28-29

END  
DATE  
FILMED  
| 81  
DTIC

(12)

LEVEL

AFGL-TR-80-0047 ✓

AD A092942

THERMOSPHERIC DIAGNOSTICS USING *IN SITU*  
PROBING BY ELECTRON-BEAM-INDUCED  
LUMINESCENCE

W.R. Pendleton, Jr.  
L.C. Howlett

Utah State University  
Logan, UT 84322

Final Report  
6/30/78 - 12/31/79

30 January 1980

Approved for public release; distribution unlimited

AIR FORCE GEOPHYSICS LABORATORY  
AIR FORCE SYSTEMS COMMAND  
UNITED STATES AIR FORCE  
HANSCOM AFB, MASSACHUSETTS 01731

DTIC  
ELECTE  
DEC 17 1980  
S B

80 12 11 004

FILE COPY

Qualified requestors may obtain additional copies from the Defense Documentation Center. All others should apply to the National Technical Information Service.

Unclassified

SECURITY CLASSIFICATION OF THIS PAGE (When Data Entered)

(9) Final rept. L  
30 Jun 78-31 Dec 79

19 REPORT DOCUMENTATION PAGE		READ INSTRUCTIONS BEFORE COMPLETING FORM
1. REPORT NUMBER AFGL TR-80-0047	2. GOVT ACCESSION NO. AD-A092942	3. RECIPIENT'S CATALOG NUMBER
4. TITLE (and Subtitle) THERMOSPHERIC DIAGNOSTICS USING IN SITU PROBING BY ELECTRON-BEAM-INDUCED LUMINESCENCE		5. TYPE OF REPORT & PERIOD COVERED Final Report 6/30/78 - 12/31/79
7. AUTHOR(s) W. R. Pendleton, Jr. L. C. Howlett		6. PERFORMING ORG. REPORT NUMBER
9. PERFORMING ORGANIZATION NAME AND ADDRESS Utah State University Logan, Utah 84322		8. CONTRACT OR GRANT NUMBER(s) F19628-78-C-0103
11. CONTROLLING OFFICE NAME AND ADDRESS Air Force Geophysics Laboratory Hanscom AFB, Massachusetts 01731 Monitor/R. R. O'Neil/ OPR		10. PROGRAM ELEMENT, PROJECT, TASK AREA & WORK UNIT NUMBERS 61102F 2310G4AM
14. MONITORING AGENCY NAME & ADDRESS (if different from Controlling Office)		12. REPORT DATE 30 January 1980
15. SECURITY CLASS. (of this report) Unclassified		13. NUMBER OF PAGES 73
16. DISTRIBUTION STATEMENT (of this Report) Approved for public release; distribution unlimited		
17. DISTRIBUTION STATEMENT (of the abstract entered in Block 20, if different from Report)		
18. SUPPLEMENTARY NOTES		
19. KEY WORDS (Continue on reverse side if necessary and identify by block number)		
Electron Beam Probe Luminescence N <sub>2</sub> <sup>+</sup> First Negative System Thermosphere N <sub>2</sub> Vibrational Temperature N <sub>2</sub> Rotational Temperature Species Concentrations N <sub>2</sub> , O <sub>2</sub> , O		
20. ABSTRACT (Continue on reverse side if necessary and identify by block number)		
The development of an electron-beam-induced-luminescence system, suitable for integration in the payload of an Astrobee F test vehicle, is described. A modified Pierce-type electron gun is used in conjunction with a magnetic lens to provide a well-defined 60-mA beam at 3.0 kV. The target emissions induced by the beam are spectrally selected and measured using a government-furnished echelle spectrometer. Initial tests of the system are described. The development of auxiliary flight instrumentation is also documented.		

DD FORM 1 JAN 73 1473

Unclassified

SECURITY CLASSIFICATION OF THIS PAGE (When Data Entered)

362850

Jm

## TABLE OF CONTENTS

	Page
REPORT DOCUMENTATION PAGE . . . . .	i
ACKNOWLEDGMENTS . . . . .	iv
LIST OF CONTRIBUTORS . . . . .	v
LIST OF FIGURES . . . . .	vi
LIST OF TABLES . . . . .	viii
INTRODUCTION . . . . .	1
SKETCH OF EXPERIMENT . . . . .	4
CONTRACTUAL OBJECTIVES . . . . .	6
DESCRIPTION OF INSTRUMENTATION . . . . .	8
Echelle Spectrometer . . . . .	8
Echelle Spectrometer Readout/Control Unit . . . . .	8
Electron Gun System . . . . .	10
Integrated Spectrometer/Gun . . . . .	18
Atomic Oxygen Detector . . . . .	20
[OI] $\lambda 5577\text{\AA}$ Photometer . . . . .	27
PERFORMANCE OF EBIL SYSTEM. . . . .	29
Electron Gun Performance . . . . .	29
Spectral Resolution of Detection System . . . . .	31
Vacuum Chamber Tests: Instrument Responsivity . . . . .	31
Background and Noise . . . . .	36
IMPLICATION OF RESULTS FOR PROPOSED MEASUREMENTS . . . . .	41
SUMMARY . . . . .	46
RECOMMENDATIONS . . . . .	47
REFERENCES . . . . .	48
APPENDICES . . . . .	49
A. Electron Gun Design Evaluation . . . . .	50
B. Specifications for Echelle Spectrometer . . . . .	65

#### ACKNOWLEDGEMENTS

The suggestions and encouragement of Robert R. O'Neil (Air Force Geophysics Laboratories) and D.F. Hansen, M.P. Shuler, Jr., and A.H. Tuttle (H.S.S., Inc.--Bedford, Massachusetts) are gratefully acknowledged. The sizable contribution of J.C. Ballard, Senior Electronics Technician, is also gratefully acknowledged.

# LIST OF CONTRIBUTORS

W.R. Pendleton, Jr.	--	Principal Investigator
L.C. Howlett	--	Co-Investigator
J.C. Ballard	--	Senior Electronics Technician
I.L. Davis	--	Graduate Assistant
K. Briggs	--	Undergraduate Assistant
S. Thorpe	--	Undergraduate Assistant

Accession For	
NTIS CB&I	<input checked="" type="checkbox"/>
DTIC TAB	<input type="checkbox"/>
Unannounced	<input type="checkbox"/>
Justification	
By	
Distribution/	
Availability Codes	
Dist	Avail and/or Special
A	

# LIST OF FIGURES

Figure		Page
1.	Conceptual Drawing of the Payload Configuration Envisioned for the Thermospheric EBIL Experiment . . . . .	5
2.	Block Diagram of Echelle Spectrometer Readout/ Control Unit . . . . .	9
3.	Electron Gun System Block Diagram . . . . .	11
4.	Fundamental Concept of Spherically Convergent Electron Gun . . . . .	12
5.	Cross-Sectional View of Convergent Beam Unipotential Electron Gun . . . . .	15
6.	Electron Gun in Pressure Tight Mounting with Explosive Cover in Place . . . . .	16
7.	Photographs Illustrating Focal Properties of the Magnetic Lens. . . . .	17
8.	Echelle Spectrometer/Gun Unit. . . . .	19
9.	Block Diagram of [0] Measurement System. . . . .	21
10.	Response of Resonant Scattering System Showing Non-linearity due to Increasing Optical Depth at High O Densities and Sensitivity Effects due to Temperature. . . . .	25
11.	Block Diagram of [OI] $\lambda 5577\text{\AA}$ Photometer. . . . .	28
12.	Cathode Current and Intensity Monitor Output <u>vs.</u> Time. . . . .	30
13.	ArI Spectra in the $\lambda 4250\text{\AA}$ Region Illustrating the Spectral Width of the Instrument . . . . .	32
14.	High-Vacuum Test Facility. . . . .	33
15.	Outputs of Echelle Spectrometer and $\lambda 3914\text{\AA}$ Intensity Monitor <u>vs.</u> Target Pressure. . . . .	35
16.	Typical Dark Signal Scans Illustrating Contributions of Reticon and Image Intensifier. . . . .	37
17.	Predicted $\text{N}_2^+ 1\text{N } (0,1) P_{\text{max}}$ Signal Growth Rate <u>vs.</u> Altitude. . . . .	42
18.	Illustration of Expected Changes in $\text{N}_2^+ 1\text{N } [I(1,2)/I(0,1)]$ with $T_V (\text{N}_2)$ : Correlation with Height-Temperature Profiles for Various Levels of Solar Activity . . . . .	43



LIST OF FIGURES (Continued)

Figure		Page
19.	Diurnal Variation of Atmospheric Temperatures at 140, 150 and 160 km During a Period of High Solar Activity . . . . .	45
1A.	Illustration of Notation Employed in the Analysis of an Idealized Spherical Flow Pierce-type Electron Gun. (Note that no attempt has been made to illustrate the required shaping of the electrodes.) . . . . .	60

# LIST OF TABLES

	Page
Table 1. Amplitude Dispersion of the $N_2^+ 1N(1,2)$ P-branch Maximum (Source pressure: $2.0 \times 10^{-4}$ torr; 150- $\mu$ m entrance slit; 1-sec integration time) . . . . .	39
Table A1. Relative Excitation Rate $R_k$ and Beam Power $P$ vs. Energy $E$ for a 1.0- $\mu$ perv Electron Gun . . . . .	56
Table A2. Space-charge Spreading of an Initially Parallel- Flow Electron Beam . . . . .	57
Table A3. Identification of Symbols used in Figure 1A . . . . .	61
Table B1. Objective Specifications of the Rocketborne Echelle Spectrometer . . . . .	65

## INTRODUCTION

The vibrational distribution of  $N_2(X^1\Sigma_g^+)$  in the thermosphere has been a topic of considerable interest and much speculation for approximately a decade. The interest stems largely from the potentially important role of vibrationally-excited  $N_2(X)$  [hereafter  $N_2^+$ ] as a latent source of energy to "drive" a number of thermospheric processes. It has been suggested that  $N_2^+$  might be the key to an understanding of a number of high-altitude phenomena which include: (i) the production of 4.3- $\mu$ m  $CO_2$  radiation in the lower thermosphere, especially under disturbed conditions [Stair, et al., 1975; Kumer, 1975]; (ii) the formation of the F-region electron density trough [Schunk and Banks, 1975]; (iii) the decrease of electron density in the  $F_2$  region in stable auroral red (SAR) arcs [Newton, et al., 1973]; and (iv) the seasonal anomaly associated with the  $F_2$ -layer [Strobel and McElroy, 1970].

In spite of the widespread interest in thermospheric  $N_2^+$ , a paucity of direct experimental results are available. It appears that ground-based auroral measurements and *in situ* measurements based on the electron-beam-induced-luminescence (EBIL) technique presently provide the most direct sources of information relating to the  $N_2(X)$  vibrational distribution in the thermosphere. Less direct information has been used on occasion to estimate the vibrational temperature of thermospheric  $N_2(X)$  [hereafter  $T_v(N_2)$ ], e.g., Kummeler and Bortner (1972).

Studies of the vibrational development of  $N_2$  and  $N_2^+$  band systems in the aurora have provided the bulk of the data relating to thermospheric  $T_v(N_2)$ . The most careful studies of *normal auroras* have consistently indicated  $T_v(N_2) < 1000^\circ K$  [Vallance Jones, 1974]. However, this persistent characteristic of the normal aurora *does not* preclude the possibility of significantly elevated values of  $T_v(N_2)$  in the thermosphere. The height-integrated (column) emission rate associated with allowed  $N_2$  or  $N_2^+$  emissions in the *normal aurora* is dominated by contributions from a relatively narrow range of altitudes in the region 100-120 km. Elevated values of  $T_v(N_2)$  at somewhat higher altitudes should affect the observed vibrational development almost imperceptibly.

The earlier AFGL/USU investigation of thermospheric  $T_v(N_2)$  [O'Neil et al., 1974], using *in situ* rocket-based EBIL probes, constitutes the most direct attempt to determine this potentially important parameter. However, limitations imposed primarily by the particular EBIL systems used in the investigation prevented the determination of  $T_v(N_2)$ . Rather, a significant altitude-dependent *upper limit* for  $T_v(N_2)$  was established in the region 80-175 km [ $T_v(N_2) \leq 800^\circ\text{K}$  for altitudes  $\leq 115$  km;  $\leq 1000^\circ\text{K}$  @ 135 km;  $\leq 1200^\circ\text{K}$  @ 155 km;  $\leq 1500^\circ\text{K}$  @ 175 km]. The experimental upper limits for  $T_v(N_2)$  appear to be consistent with the results of the more recent theoretical computations, but actual determinations of  $T_v(N_2)$  in the thermosphere are urgently needed to provide "benchmarks" for ionospheric and thermospheric models.

The experimental data for quenching of  $N_2^+$  by O have established this process as the dominant loss mechanism for thermospheric  $N_2^+$  over a moderate range of altitudes and atmospheric conditions. Cooling of  $N_2^+$  by  $\text{CO}_2$  is expected to be competitive with cooling by  $\text{O}(^3\text{P})$  at altitudes  $\lesssim 110$  km, and diffusion is expected to dominate the vibrational loss rate at altitudes  $\gtrsim 200$  km. The primary impact of the O-quenching process is to hold the  $N_2(X)$  vibrational temperature near the gas-kinetic temperature in most model calculations. However, recent analyses by Torr and Sharp (1979) indicate that low O concentrations in the aurora are typical, and mean [O] values are about a factor of 2.5 lower than those of the CIRA 1965 model atmosphere. [This result is consistent with an auroral-zone [O] measurement by USU which yielded peak O densities of  $<10^{11}\text{cm}^{-3}$  (Howlett, Pendleton, and Shaw, 1979).] The use of these reduced O densities in model calculations of thermospheric  $T_v(N_2)$  yields a diurnal maximum  $N_2(X)$  vibrational temperature of  $\approx 1000^\circ\text{K}$  at an altitude of 150 km. This result is consistent with the estimate of Brieg et al. (1973) for reduced oxygen concentrations and a significant  $\text{O}(^1\text{D})$  contribution.  $N_2(X)$  vibrational temperatures of this magnitude at 150 km are expected to yield unambiguous temperature measurements using the EBIL technique.

The present report documents research and development efforts conducted by Utah State University under contract F19628-78-C-0103. The primary thrust of the R&D effort was toward the development and testing of a rocket-based EBIL system for *in situ* thermospheric measurements of  $T_v(N_2)$ ,  $T_r(N_2)$ ,  $[N_2]$ ,

[O<sub>2</sub>], and [O]. The primary and ancillary hardware items developed under the contract are described. The performance evaluations of the EBIL system, which includes the government-furnished rocket spectrometer, are documented. The test results are interpreted in terms of the proposed thermospheric measurements, and recommendations are made for system improvement to enhance the probability of obtaining the desired results.

## SKETCH OF EXPERIMENT

The general concept of the proposed prime experiment is depicted in Figure 1. Following payload separation, orientation, and stabilization by  $\approx 110$  km on the ascent portion of the trajectory, a focused, energetic beam of 3.0-keV electrons is injected into the surrounding medium by means of an electron gun. The interaction of the electron beam with the atmosphere induces optical emissions which are quantitatively analyzed with the echelle spectrometer system to ultimately effect temperature and species concentration determinations. The effective optical axis for the detection system is canted at a small angle with respect to the beam, which is directed antiparallel to the geomagnetic field. The effective test sampling region is then defined by the intersection of the spectrometer field-of-view and the electron beam (cross-hatched region) in Figure 1. Assuming an ideally stabilized payload, the location of the observation region along the beam axis remains fixed. The final selection of the observation region will be dictated primarily by considerations of instrument sensitivity and of possible distortion of the sample properties by the motion of the measuring device and the vehicle itself.

The anticipation of low S/N ratios at high altitudes, where  $T_v(N_2)$  is expected to be high enough to produce a significant ( $\approx 10$ -20%) departure of the  $N_2^+IN$  intensity ratio  $[I(1,2)/I(0,1)]$  from the "cool ratio", suggests that the flight apogee be selected to maximize the measurement time in the most favorable altitude region. Arguments which will subsequently be presented identify a desired flight apogee of  $\approx 150$  km.

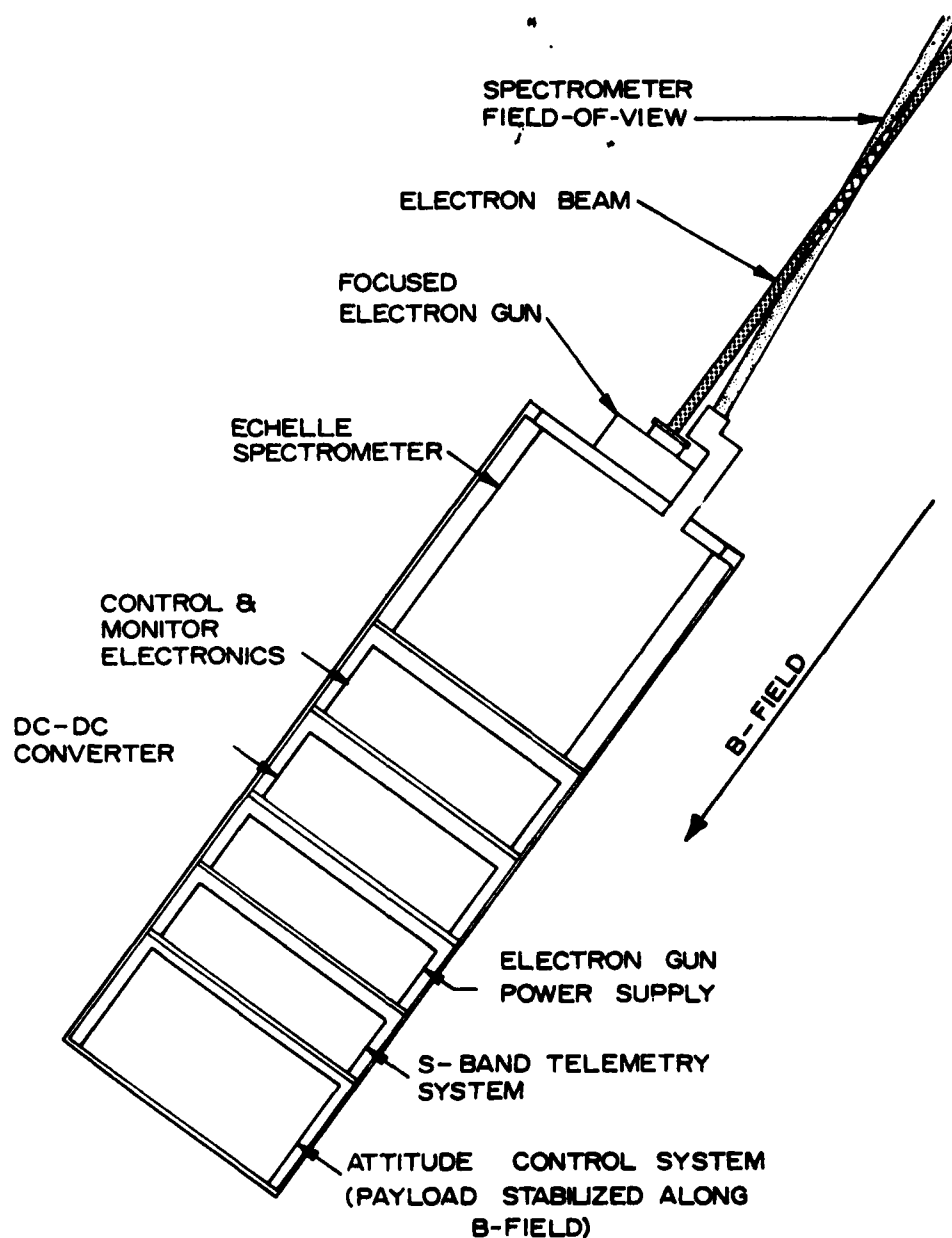


Figure 1. Conceptual Drawing of the Payload Configuration Envisioned for the Thermospheric EBIL Experiment.

## CONTRACTUAL OBJECTIVES

The basic objectives of the research and development described in this report are summarized below.

1. Perform necessary research to design, fabricate, test and integrate a rocketborne electron beam source with the specifications called out in 2.
2. Study various electron beam source design options to maximize the photon emission rate of electron-beam-induced atmospheric radiations as viewed by a rocket-based  $f/2$  echelle spectrometer. Design trade offs include electron beam energy, current and cathode/anode configuration. Major considerations are:
  - a. Maximize the  $f/2$  spectrometer optical throughput.
  - b. The electron source operating altitude extends from 100 to 200 km.
  - c. The minimal effective photon emission rate within 1 meter distance near the payload is equivalent to or greater than that produced by a 3 kV, 50 mA electron beam.
  - d. The electron beam must be capable of beam shut off for several seconds three times during the course of the six minute experiment.
  - e. The electron beam energy and current must be constant within plus or minus ten percent of the normal operating parameters during the experiment.
3. Integrate the electron beam unit and the government-furnished rocket spectrometer in a configuration suitable for use with an Astrobe-F sounding rocket.
4. Test the gun/spectrometer system.



As an outgrowth of discussions with the technical monitor, the objectives were expanded to include the development of an atomic oxygen resonance fluorescence system for [O] measurements and a related [OI]  $\lambda 5577\text{\AA}$  photometer.

## DESCRIPTION OF INSTRUMENTATION

### Echelle Spectrometer

The rocketborne echelle spectrometer was developed by H.S.S., Inc. of Bedford, Massachusetts under a separate contract. The instrument has been described in detail by Hansen et al. (1978). The objective specifications, as documented by Hansen et al., are included for convenience in Appendix B of this report.

The research and development efforts summarized herein have been directed toward meeting the contractual objectives listed in the preceding section. Optimization of the performance of the spectrometer was not identified as an item for contractual effort, but the instrument evaluations described in the next section clearly reveal the need for additional effort toward this end.

It became apparent at an early stage of the program that a digital readout/control unit was needed for convenient operation and evaluation of the spectrometer. The device which evolved is described in the next subsection.

### Echelle Spectrometer Readout/Control Unit

The echelle spectrometer provides several outputs which must be interpreted in order to obtain a measurement. Additionally, there are several control inputs that must be sent to the spectrometer to establish the desired operating mode. These readout and control requirements made it necessary to construct a device to establish a convenient means for an operator to communicate with the instrument. The block diagram of this device is shown in Figure 2.

The analog signal from each element is digitized to 10-bit accuracy to form a ten line parallel data bus along with status lines identified as data valid and data ready. Additionally, the integration time for the measurement is sent out on a ten line bus, and a separate two line bus monitors which order sorting filter is in place.

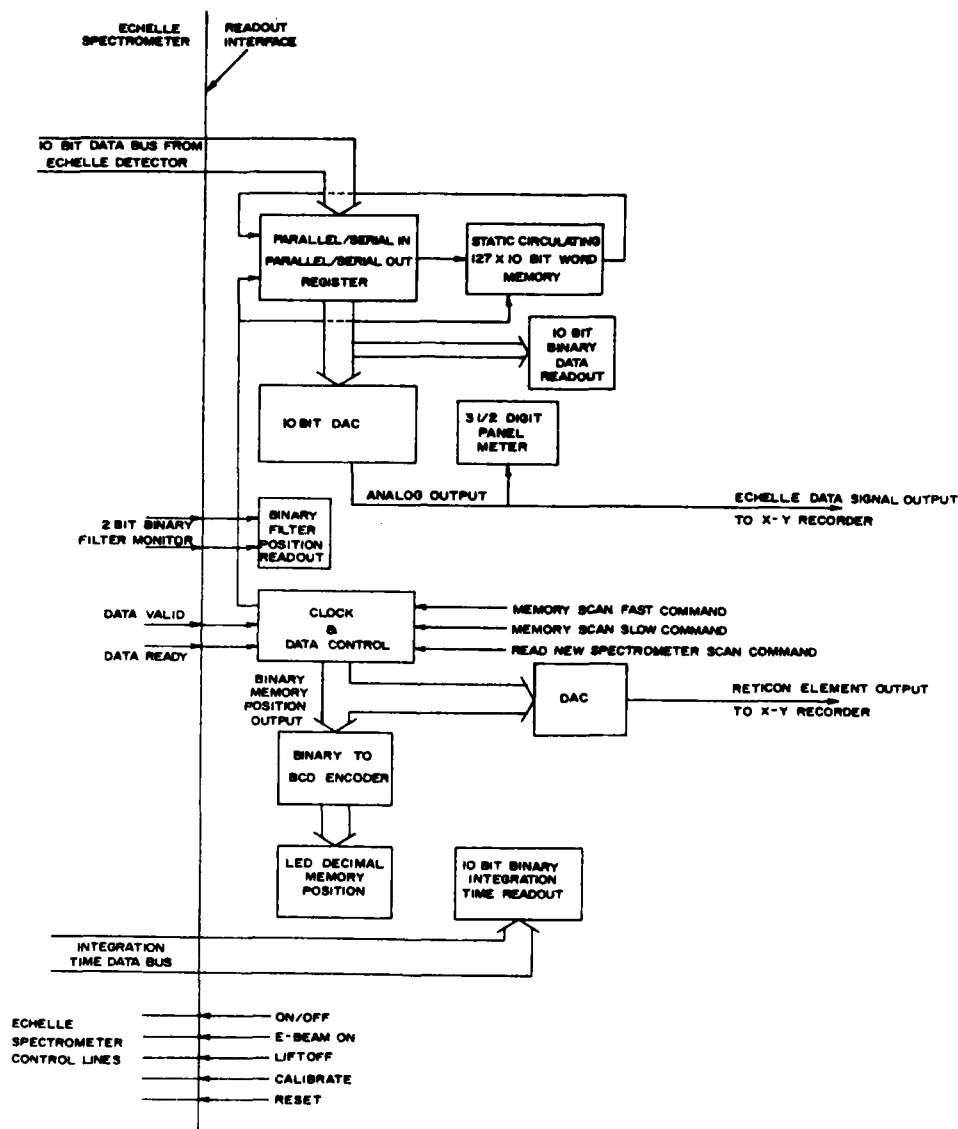


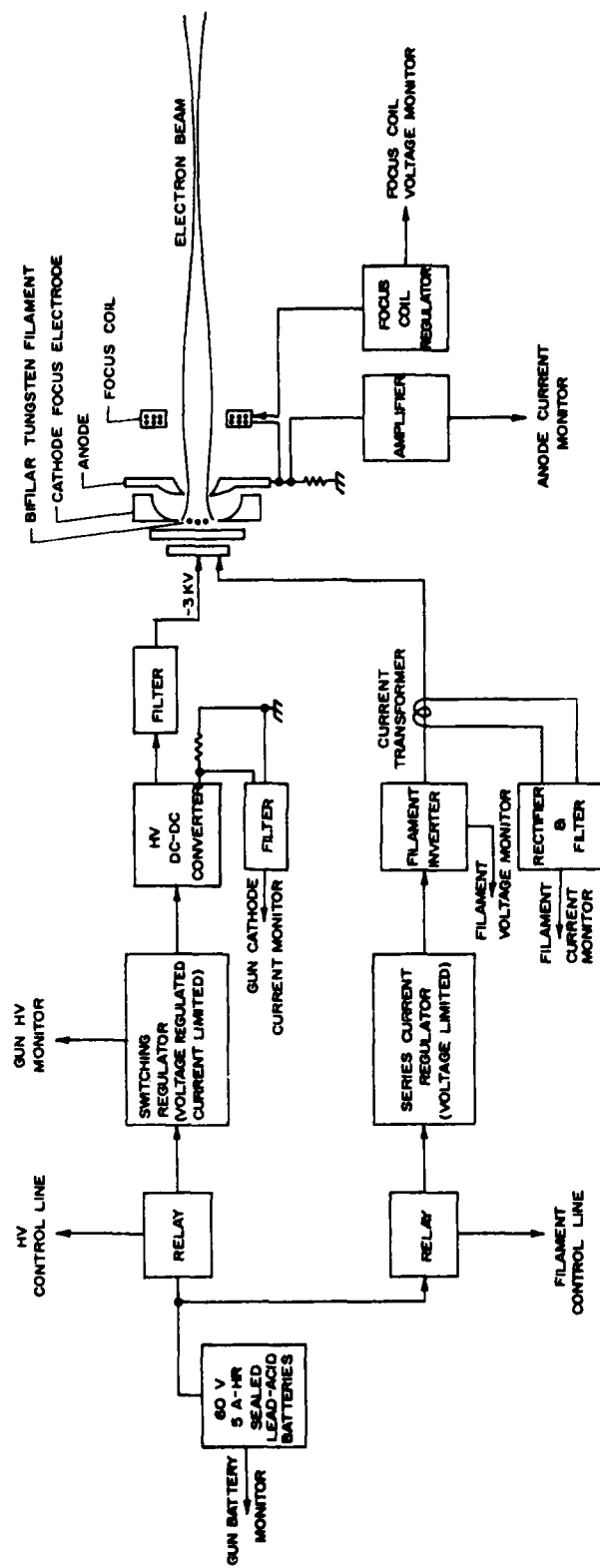
Figure 2. Block Diagram of Echelle Spectrometer Readout/Control Unit.

The data readout device is designed to accept a spectrometer scan of data and store it in a memory which may be circulated to examine a desired data word (corresponding to any desired Reticon diode). This memory is read out in binary (for maximum accuracy), in decimal (for maximum human intelligibility), and as a voltage for plotting on an X-Y recorder. The Reticon element number is similarly presented both as a decimal digital display and as a voltage for plotting. The order-sorting filter position is read out in binary code. Also, all of the spectrometer control functions may be exercised from the data readout unit. The memory may be circulated at two different rates for convenience in finding a desired element or for X-Y plotting of an entire spectrometer scan.

#### Electron Gun System

The electron gun system is required to produce a well-focused beam of electrons at about 50 mA and 3 kV. It must also be insensitive to contamination (poisoning) from exposure to normal atmospheres either when cold at full pressure or when hot at a pressure  $\approx 10^{-3}$  torr. It should also be serviceable in the field, if necessary. The associated power supplies should be efficient in the use of power and weight as well as cost. Experience has also shown that the power electronics must be capable of surviving arcs within the gun or even short circuit operation, without failure. All significant gun operating parameters must also be monitored.

Numerous approaches to the system design were considered and evaluated. The scheme shown in Figure 3 resulted. The electron gun itself follows the design philosophy outlined by Pierce (1940, 1949). If a hollow sphere is considered as shown in Figure 4, which emits electrons from its inside wall and the electrons are collected at the center, electron trajectories (assuming zero velocity when emitted) will be straight and will converge to the center point. If a circular segment of the spherical surface is considered alone, the beam of electrons forms a cone having an apex at the sphere center. Electrons within the isolated cone will have the same trajectories as those within the sphere if the potential distribution along the cone boundary is the same whether the cone is an imaginary segment of a sphere or standing alone. If electrodes outside of the convergent conical electron



ELECTRON GUN SYSTEM

Figure 3. Electron Gun System Block Diagram.

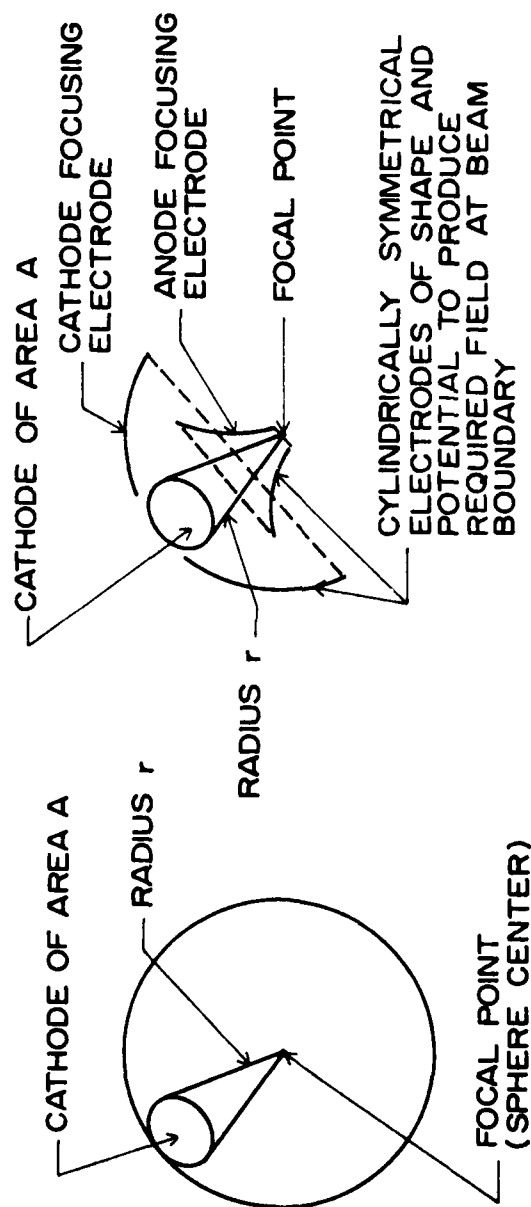


Figure 4. Electrons emitted from area A on the inside surface of a spherical cathode form a conical beam with its apex at the center of the sphere. With proper selection of electrodes and potentials, the same boundary conditions at the conical beam edges may be obtained with the resulting convergent beam being identical to that of the spherical cathode.

beam are shaped in such a manner as to produce the proper potential along the cone boundary the electrons will be focused to a point at the apex of the cone with virtually 100% efficiency, i.e., no current flow to the focus or accelerating electrodes.

If a diverging lens could be placed in the converging beam between the cathode and focal point, the converging beam could be made parallel. This is accomplished by the exit aperture in the anode focusing electrode acting as a single-aperture electrostatic lens due to the field equipotential lines within the gun bulging out through the aperture into the field free region outside the gun.

A more thorough analysis of the convergent unipotential electron gun reveals that the gun should be operated in the perveance rather than emission limited mode. In this case the beam current is related to the acceleration voltage to the  $3/2$  power. The focusing characteristics are independent of accelerating voltage. Both the focusing into a parallel beam and the maintenance of a conically converging beam inside the gun are determined experimentally within theoretically established guidelines or by numerical computer models.

The electron gun developed at USU was based on a  $15^\circ$  (half angle) convergent beam and exit aperture lens to produce a roughly parallel or slightly divergent exit beam. A pure tungsten, bifilar-wound, plane filament was found most successful. Pure tungsten is least affected by poisoning but has several drawbacks which had to be considered. First, it requires a temperature of between 2100 and 2200°K to produce sufficient emission to ensure perveance-limited operation. This requires about 120 watts of power which must be dissipated. The heating of elastomer seals within the gun limits continuous operation to in the order of 10 minutes. The high filament temperature also produces a high light level, which has proven a mild hindrance during tests with the echelle spectrometer conducted in a vacuum chamber. Finally, tungsten recrystallizes after high temperature operation and becomes more brittle and subject to breakage from shock. This can be almost totally eliminated by using an alloy of 97% tungsten and

3% rhenium. The alloy has the emissive and electrical properties of pure tungsten but remains ductile. Some preliminary tests were conducted with filaments made from this alloy, but the samples were not stress relieved at a sufficiently high temperature to preserve dimensional stability at 2100°K. If pure tungsten filaments prove mechanically unsatisfactory, the alloy filaments could be used with proper annealing. The bifilar filament winding was required to eliminate distortion of the electron trajectories by the magnetic field associated with the filament current.

The electron gun depicted in cross section in Figure 5 was designed so that it could be readily disassembled for filament replacement or adjustment of electrode configuration. The gun is sealed so that the entire back portion can remain at atmospheric pressure at all times to prevent arcing. The front anode is provided with an o-ring seal so that a cover can be fitted allowing the inside of the gun to be pumped and sealed prior to flight. While pumping, the gun may be operated for short periods of time. The cover, which is shown in place in Figure 6, is spring loaded and is retained by a wedge and single screw. When the screw is cut by a guillotine, the gun cover is ejected to the side.

Since the gun characteristics are 100% geometry controlled, adjustability becomes very difficult since machining operations would be required. To provide adjustability for optimizing the beam shape, a magnetic lens was positioned near the anode of the gun. This allows the beam to be focused at any desired point from infinity (or diverging) to within an inch or two beyond the magnetic lens. A variety of focus conditions are shown in the photographs of the beam-induced emissions in Figure 7.

The power conversion system for the electron gun, as shown in Figure 3, starts with a 60 V, 5 A-hr battery pack. Sealed Gates lead-acid cells were chosen because of their proven performance in flight, freedom from outgassing on either charge or discharge (unless grossly abused) and cost. This battery pack is totally dedicated to the electron gun and is isolated from all other power or signal sources. Battery power is fed through a pair of relays (controlled by payload timers) to regulators for both a high voltage converter and a filament inverter.

The high voltage DC-DC converter uses a dual-core design with a relatively small saturating core controlling the drive for a larger tape-wound power core. This prevents the power core from saturation and thus



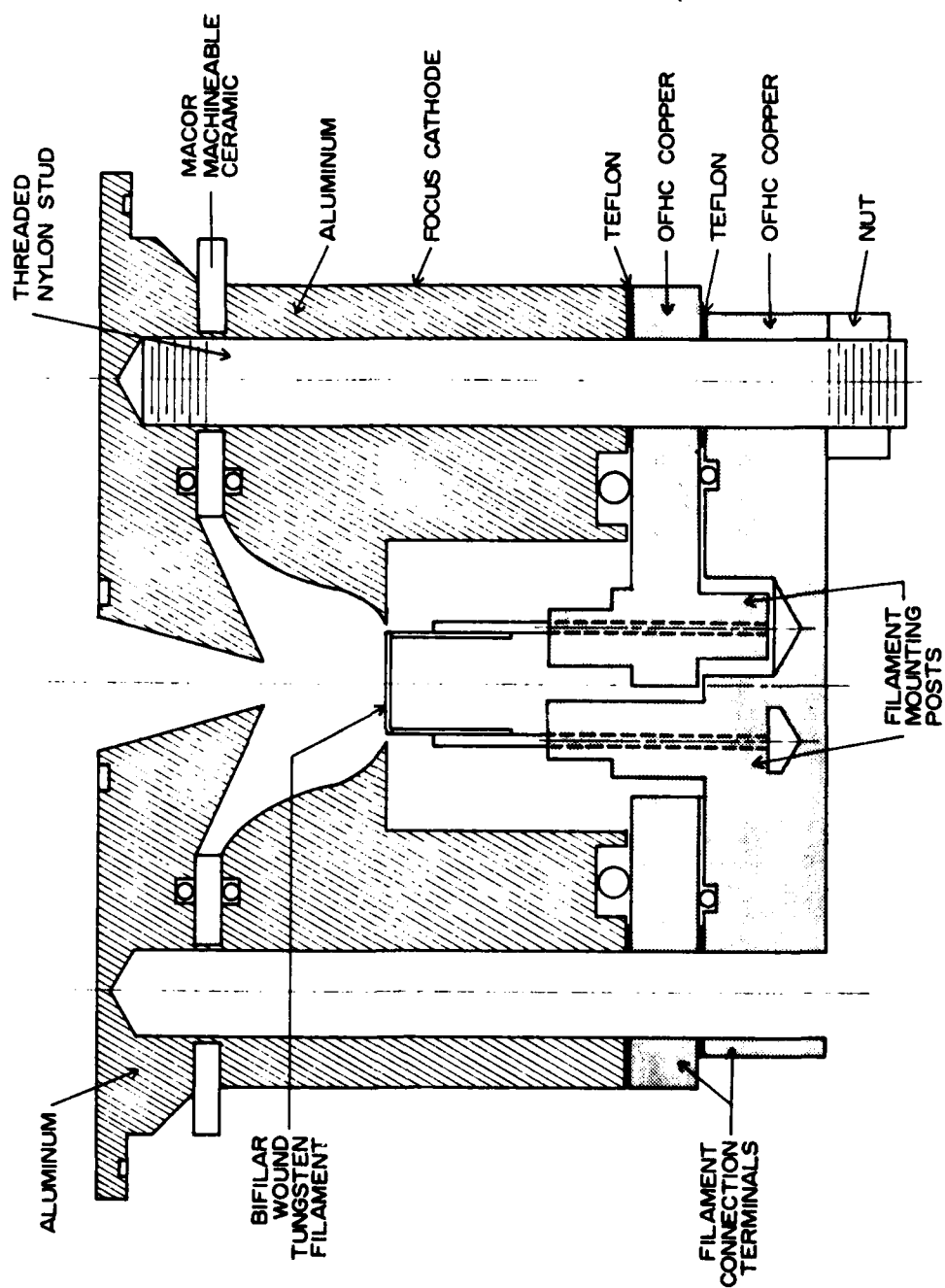


Figure 5. Cross-Sectional View of Convergent Beam Unipotential Electron Gun.

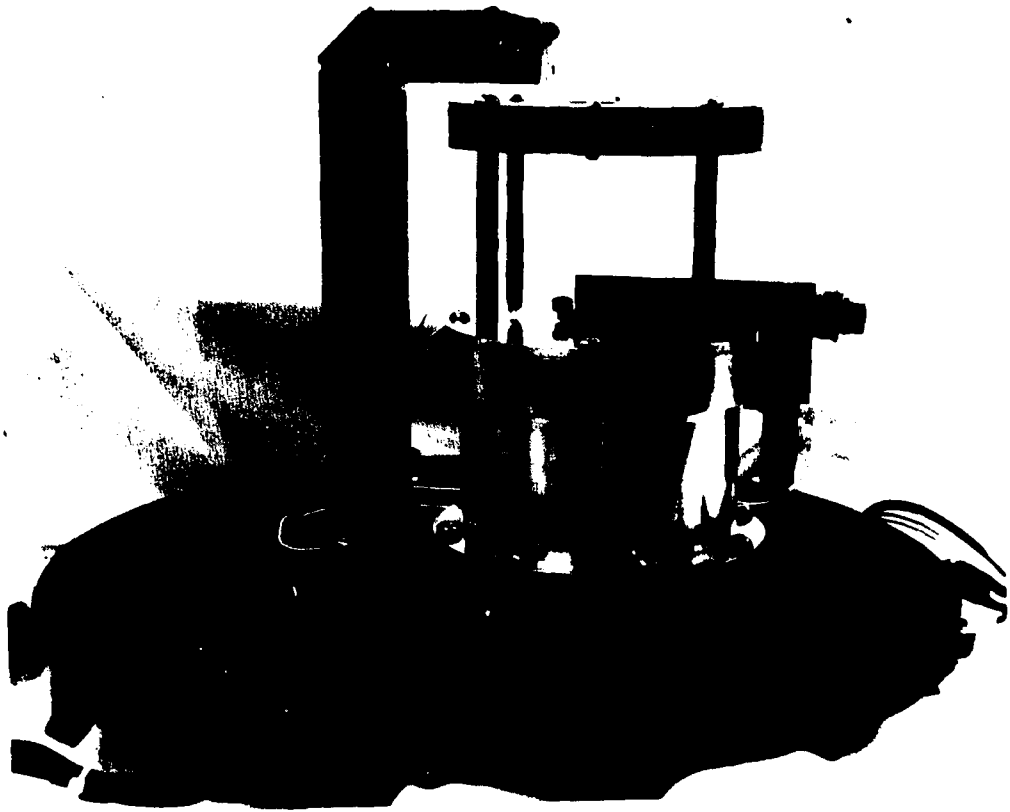


Figure 6. Electron Gun in Pressure Tight Mounting with Explosive Cover in Place.

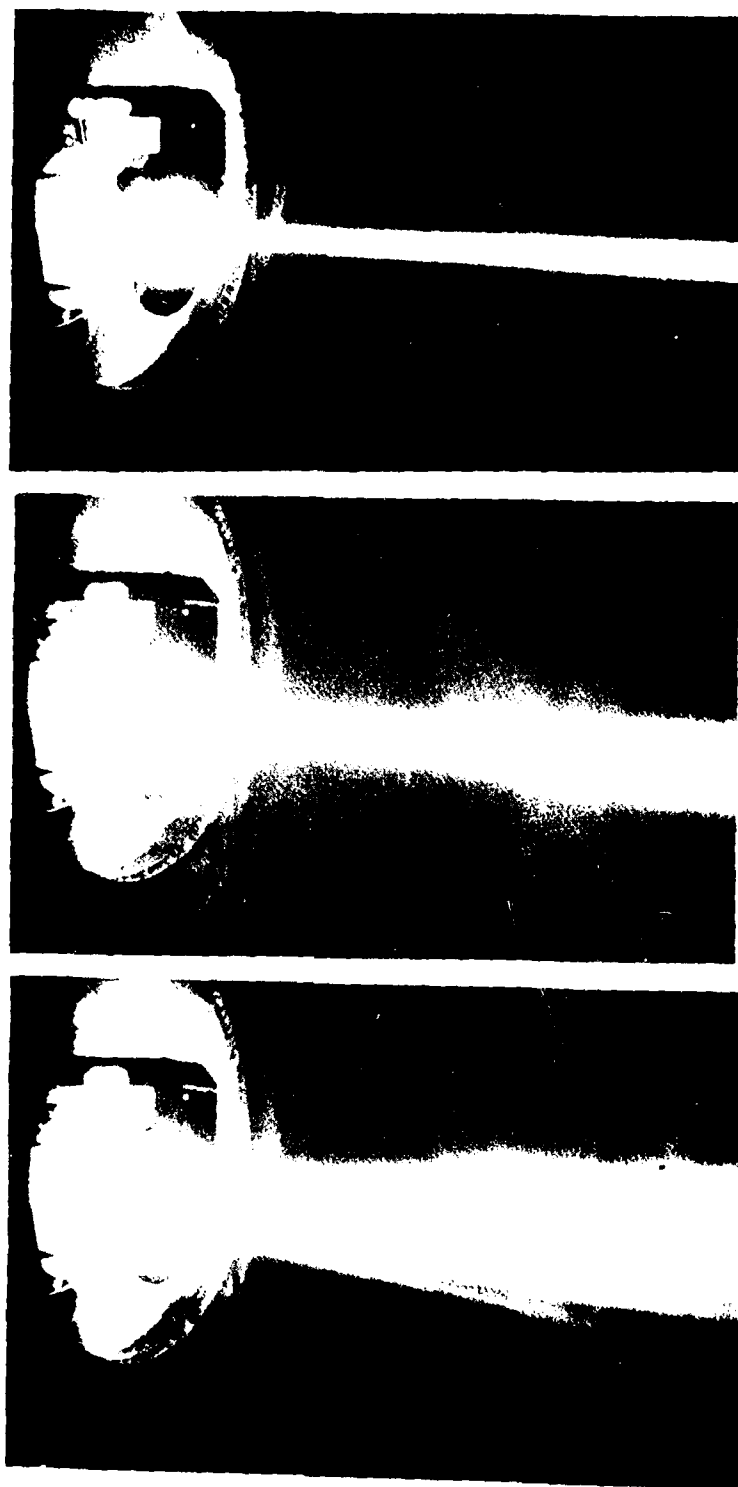


Figure 7. Photographs Illustrating Focal Properties of the Magnetic Lens.

maintains higher efficiency. All power transistors are protected from both normal and arc-related transients by zener diodes. The converter output is bridge-rectified and filtered by a two-section choke input filter so that under full load the ripple is less than 1%. The return current, which must equal the cathode current, is monitored through a resistor to provide a measure of the filament emission.

The high voltage converter is supplied from a voltage regulated, current limited switching regulator. Under normal conditions only the voltage regulation would be required; however, under abnormal conditions the current limiting will allow the converter to survive. Energy storage in the form of capacitance at the preregulator output is limited to in the order of 0.5 joule to insure that the converter semiconductors could not be damaged by stored energy.

The filament inverter is a more traditional high frequency ( 20 KHz) saturating ferrite-core design powered from a series-pass current regulator. This regulator is also voltage-limited to control the amount of power which may pass. The current limiting greatly reduces the surge currents during filament warm-up. The filament current is monitored by a current transformer feeding a rectifier and filament. Filament voltage is less directly monitored by a rectified, filtered output from a separate inverter winding.

The total current drain from the 60 Volt batteries for both the filament and high voltage is approximately 9.5 Amps giving over 30 min of battery life. Since neither the filament nor high voltage will be on until well into the flight, the power reserve is much more than adequate.

#### Integrated Spectrometer/Gun Unit

The echelle spectrometer and electron gun were integrated into a measurement system as shown in Figure 8 . This system design was governed by the need to place the spectrometer field-of-view near the electron beam and to look nearly parallel to the beam direction. Other considerations were the desirability of keeping the image intensifier at atmospheric pressure and the absolute requirement of keeping all gun high voltage points at full atmospheric pressure. The batteries, on the other hand, are not hurt by exposure to vacuum over a flight period and could be extremely damaging to the spectrometer if shorted or ruptured during recovery.

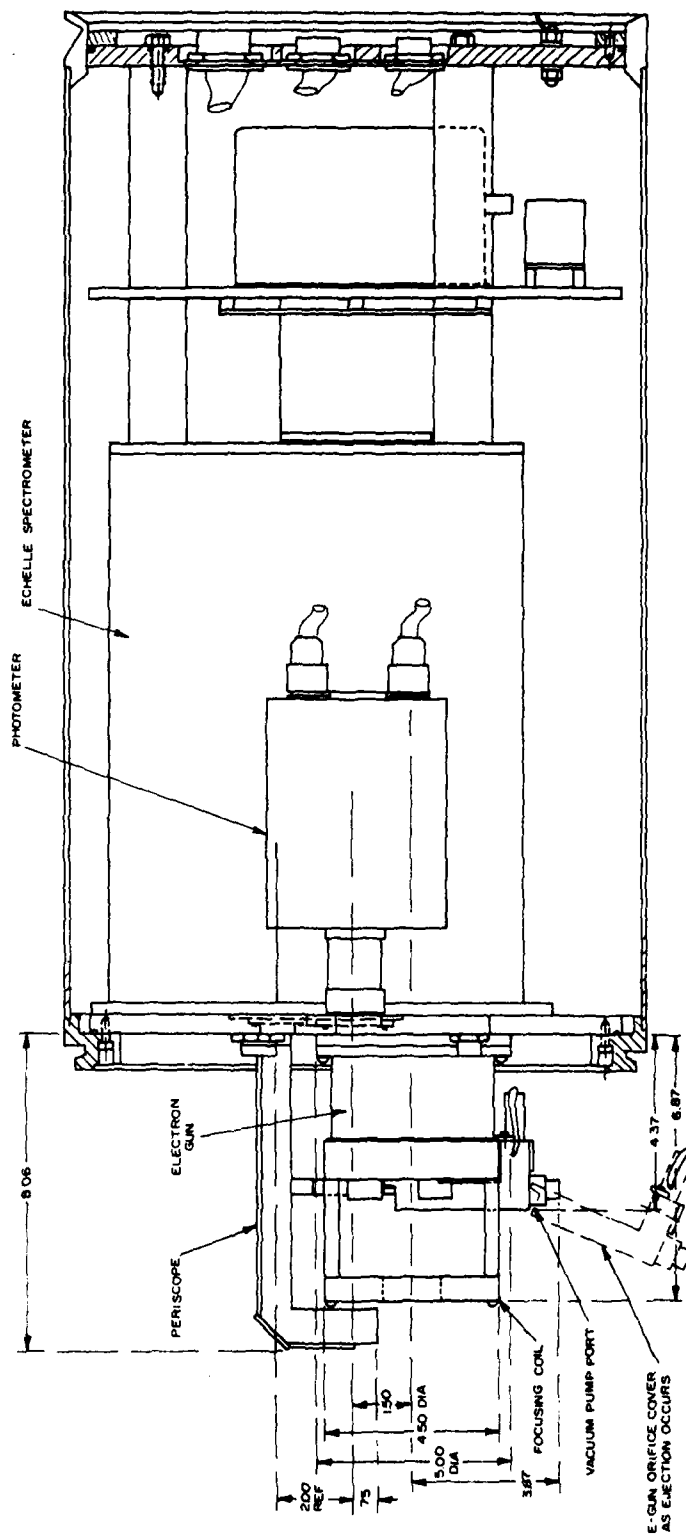


Figure 8. Echelle Spectrometer/ Gun Unit.

To best satisfy the above considerations, we elected to house the echelle spectrometer and gun power converters in a pressure-tight section sealed at atmospheric pressure and to mount the battery pack in an unpressurized section with the remaining instrumentation and payload control.

The proper positioning of the spectrometer field-of-view with respect to the electron beam was accomplished by a pair of mirrors enclosed within a light-tight mounting to form a sort of periscope. The final mirror could be tilted to any desired position to direct the field-of-view at the desired angle across the electron beam.

The photon counting photometer, although able to operate in vacuum, was placed alongside the spectrometer and viewed vertically through a window.

#### Atomic Oxygen Detector

The system for measuring atomic oxygen was based on the measurement of light resonantly scattered from ambient atomic oxygen (Figure 9). The source of the light is an rf-excited oxygen resonance lamp which is collimated to provide a beam impinging on the atmosphere. A portion of the beam is resonantly scattered by the ambient atomic oxygen into a photon detector viewing a segment of the beam. The effective cross section for the resonant scattering of the  $1304\text{\AA}$  resonance lines is large ( $\approx 10^{-14}\text{ cm}^2$ ) thereby providing a substantial return signal. This large return signal is important for the reduction of effects of atmospheric background emissions including  $1216\text{\AA}$  H Ly- $\alpha$ . Since the interfering light sources are relatively steady, the lamp was square-wave modulated so that the background (lamp off) could be subtracted from the signal plus background (lamp on).

An atomic oxygen resonance lamp requires that many considerations be met. Since atomic oxygen is very reactive, it is virtually impossible to achieve stable operating conditions in a simple sealed system. A discharge in pure oxygen requires far too high a pressure so that the atomic oxygen emissions are optically thick, resulting in reversed lines. If an inert carrier is added to establish a favorable discharge pressure while allowing a very low oxygen partial pressure, conditions are much improved, but

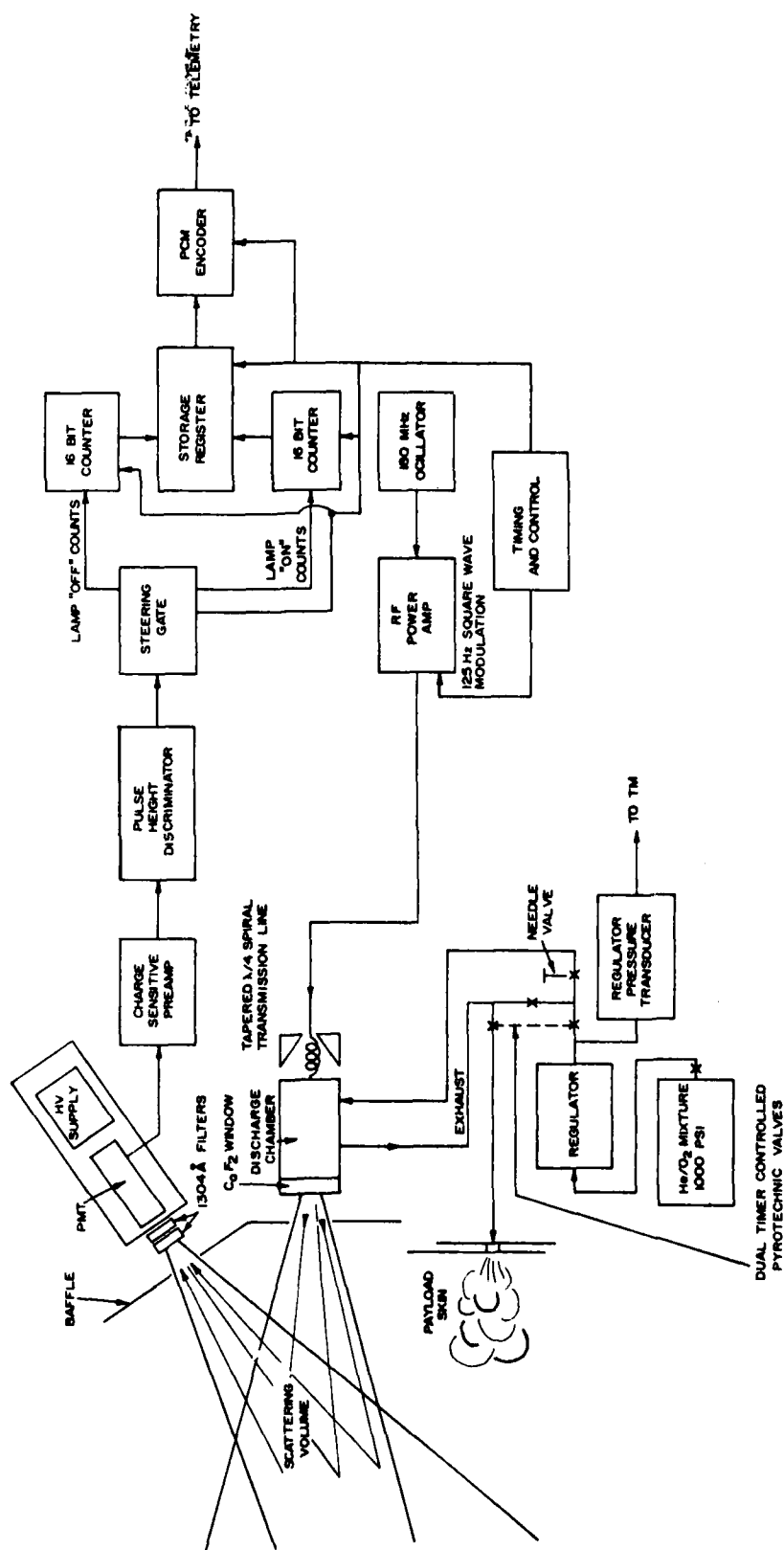


Figure 9. Block Diagram of [O] Measurement System.

unstable, because both  $O_2$  and especially  $O$  are easily gettered by chemical combination on the walls of the chamber when there is a discharge. At the same time, oxygen is being introduced into the chamber as an outgassing product from the walls.

The approach to the resonance lamp design is to establish an rf-discharge in a coaxial chamber with a flowing mixture of helium and oxygen such that the flow rate is fast enough that the gas composition in the discharge is almost totally independent of both gettering and outgassing. The  $He/O_2$  mixture, which can be in any desired mixing ratio for optimum performance, is stored in a sample cylinder at about 1,000 psi. The mixture is regulated to about 25 psi, bled through a needle valve, and then passed through the discharge chamber, finally venting to the atmosphere. The needle valve allows the discharge pressure to be set at any desired value between  $\approx 0.1$  and 50 torr for optimum operation. Prior to flight, the discharge chamber is filled at the final operating pressure and sealed by (explosive-actuated) valves at both the inlet and exhaust. As soon as the payload reaches an altitude where the ambient pressure is small in comparison with the desired discharge pressure, the valves are opened and the flow begins with a minimal transient in chamber pressure.

The discharge is powered at approximately 180 MHz by an rf oscillator driving a buffer amplifier, which in turn drives a power amplifier module. The rf is fed to a spiral tapered transmission line  $\lambda/4$  long. This resonant length builds the voltage to a sufficient level to produce the discharge. The power amplifier module has provision for a drive control. A suitable drive control permits both power control and square-wave modulation.

A  $CaF_2$  window over the discharge chamber was selected because its short wavelength cutoff was sufficiently sharp to give good transmission at  $1304\text{\AA}$  while providing adequate rejection of  $H\text{ Ly-}\alpha(1216\text{\AA})$ . During actual operation  $1216\text{\AA}$  emission from the lamp would be of no consequence. However, it would be potentially troublesome during calibration. Also, this emission could in principle contribute to the reading of a lamp intensity monitor, thus complicating the interpretation of the reading.

The  $1304\text{\AA}$  lamp emissions are the only lines for which it is desirable to have a good monitor of intensity. To monitor this output to the exclusion of virtually all other emissions, an ionization chamber was constructed having



a NO fill and  $\text{CaF}_2$  window. The ionization potential of NO prevents ionization by any significant emitters other than O and H. The H emission at  $1216\text{\AA}$  is rejected by both the  $\text{CaF}_2$  window on the lamp and the  $\text{CaF}_2$  window on the ionization chamber. There are oxygen emissions at  $1304\text{\AA}$  and  $1356\text{\AA}$ , both of which will be transmitted by the window. Both of these emissions will ionize NO and contribute to the signal from the monitor. Fortunately, the longer-wavelength emission is weaker and is detected with a significantly lower efficiency. Hence, for all practical purposes, only the O resonance triplet is measured.

The detector used to measure the resonantly scattered signal is a solar blind EMR 541G photomultiplier preceded by a  $1300\text{\AA}$  interference filter. Although the EMR photomultiplier is blind to solar radiation on the ground, it has a significant sensitivity to the ultraviolet wavelengths absorbed by the earth's lower atmosphere, which are present in the regions of interest for atomic oxygen measurements. To further reduce the sensitivity to UV radiation, a  $1300\text{\AA}$  filter is used in the head of the photomultiplier. This filter is not very good by visible standards, having a transmission of about 20% at  $1300\text{\AA}$  with about a  $200\text{\AA}$  FWHM bandwidth, but it does substantially increase the rejection of middle ultraviolet radiation.

To provide optimum sensitivity, linearity, and dynamic range, the photomultiplier is operated in a photon-counting mode with a charge-sensitive preamplifier followed by a 20-ns differentiating filter prior to pulse height discrimination. Accepted pulses are "steered" to appropriate counters, depending on whether the lamp is "on" or "off". The "on" and "off" count rates are accumulated for 20 ms each and then telemetered to ground in a PCM format.

The conversion of an observed count rate to a quantitative atomic oxygen density requires some type of calibration. One approach which sounds simple and direct--to operate the instrument in a accurately known atomic oxygen environment, is a formidable problem. Another approach, which is the one taken by USU, is to model all of the physical parameters of the system to derive a "transfer function" between photon count rate and atomic oxygen concentration from fundamental physical parameters.

The geometrical parameters of the system include the lamp and detector diameters, baffle apertures and separation distances between the baffles and

detector and lamp, and the angle and separation distance between the lamp and detector. Additionally, the directional character of the lamp itself must be taken into account.

Physical considerations are handled separately for each of the three lines in the O resonance triplet taking the line height ratios measured for the particular lamp which was flown. Assuming an effective emission temperature with only Doppler broadening, an effective cross section for an absorber can be calculated from the absorber temperature (which enters into both the convolution of the emission and absorption line shapes and also into the population distribution of the ground-state absorbers) and optical depth along the path from the lamp to the scattering volume in question. This generates a source function (energy absorbed per unit of volume) over the volume of the lamp beam as determined by the lamp baffle. This source function produces the photons which result in the return flux at the detector.

In the region where the conical lamp beam and detector field-of-view intersect, single scattering only is considered, but conservation of photons is required as an approximation of multiple scattering effects. In the region of lamp beam before the detector field-of-view is reached, only double scattering is considered. All of the sources are then numerically integrated to produce a total detected flux as a function of atmospheric temperature and atomic oxygen density. The results of these calculations are shown in Figure 10.

Two things are immediately obvious from Figure 10. A non-linear saturation effect occurs at high densities, and the scattering process is temperature sensitive. The non-linearity at high densities is caused by: 1) the scattering of photons out of the beam defined by the lamp and its baffle, 2) reduction of the effective scattering cross section as the emission line becomes more and more reversed, and 3) reduction of the probability that a scattered photon will make its way back to the detector because of further scattering. The temperature dependence reflects two effects: (1) line overlap in emission and (subsequent) absorption and (2) the population distribution among the fine structure terms in the  $^3P$  ground state of O.

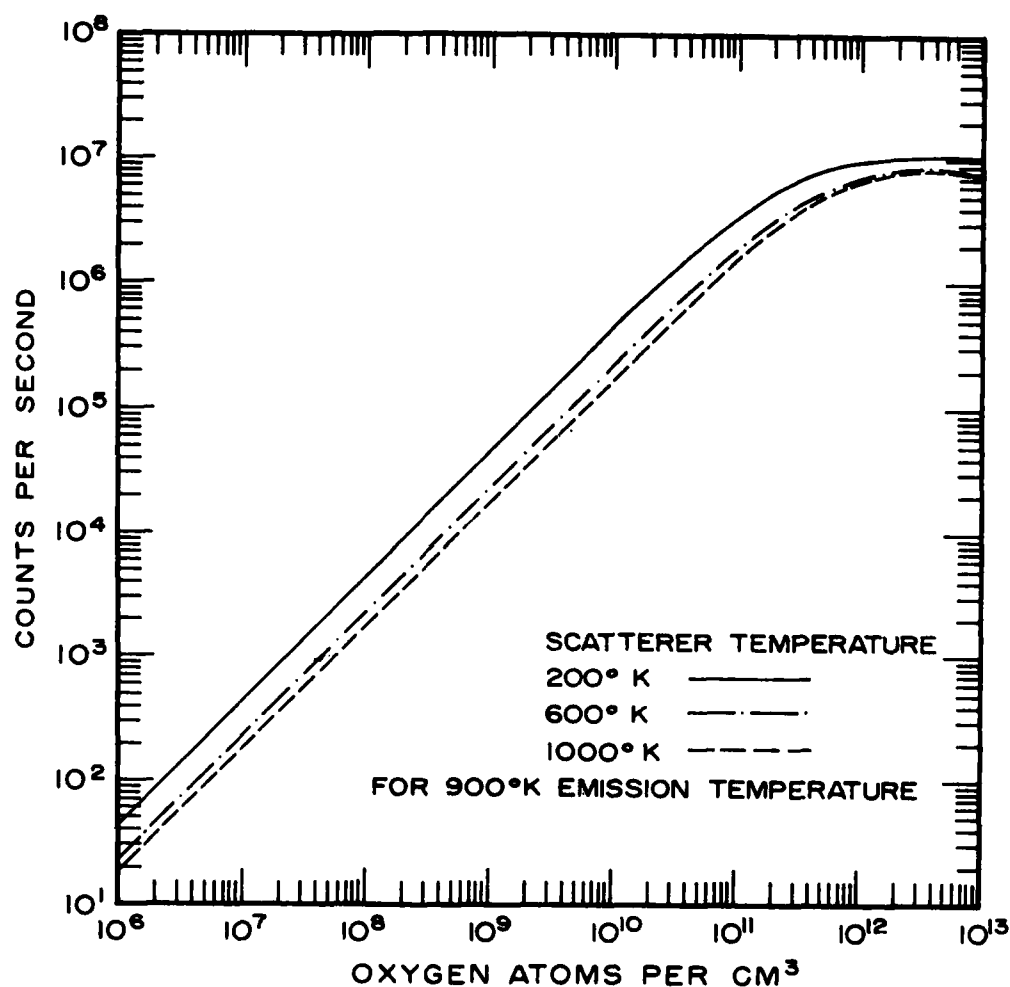


Figure 10. Response of resonant scattering system showing non-linearity due to increasing optical depth at high O densities and sensitivity effects due to temperature.

The modeling process considers an assumed lamp intensity, and 100% detection quantum efficiency, neither of which are anywhere near correct. Since the detected count rate varies linearly with both the lamp intensity and quantum efficiency, neither need be known, but only their product. The product can be measured with high accuracy by determining the response of the detector to the lamp when the two are separated by a known distance in a vacuum environment.

### [OI] 5577Å Photometer

The altitude profile of zenith 5577Å airglow emission is very useful as a comparison against the electron beam probe measurement of atomic oxygen and the resonant scattering O measurement. In order to successfully perform the required spatial differentiation of the 5577Å altitude profile, it is necessary to have a photometer that is both exceptionally sensitive and quiet. Since the column 5577Å airglow intensity is in the order of 200 R, a sensitivity and noise level with a 1-sec measurement time would need to be about 1 R, if possible. With premium components the performance can be calculated from two limiting factors--photomultiplier dark count rate and the  $\approx 3/4$  R/Å background that exists from all other sources. With a 15Å FWHM filter the background will be somewhat over 10 R. Assuming a detector area of  $2.68 \times 10^{-1} \text{ cm}^2$  a 40% peak filter transmission,  $\approx 20\%$  detector quantum efficiency,  $5^\circ$  half angle field-of-view, 100 counts/sec background count rate due to dark emission from the photocathode, the detection system would have a background of  $\approx 1.25$  R which is small in comparison with natural sources. Signal-to-noise which will ultimately determine the accuracy with which a spatial differentiation could be performed should be determined by photoelectron Shot noise at the photocathode. A 1-sec integration time measurement at 10 R (background level) should have a rms noise deviation of  $\approx 4\%$  or better. This signal-to-noise ratio should improve even more at higher signal levels.

Since the anticipated sensitivity is in the order of 82 counts/R sec a 300-R airglow level would produce a count rate of  $2.5 \times 10^4$  counts/sec which is easily within the  $\approx 6 \times 10^6$  counts/sec limit of the electronics.

The photometer block diagram of Figure 11 shows the essential features of the photometer. The photomultiplier (EMR 541N) is run at about  $10^7$  gain and drives a charge-sensitive preamplifier. The resulting pulses have approximately 20 ns rise times and 200 ns fall times. The charge-sensitive preamplifier drives a passive differentiating filter having a 30 ns time constant, a comparator is used to discriminate out any power supply noise and to avoid double counting of a single pulse. Accepted pulses are counted for 240 ms and are encoded into a 100 pps PCM format for telemetry.

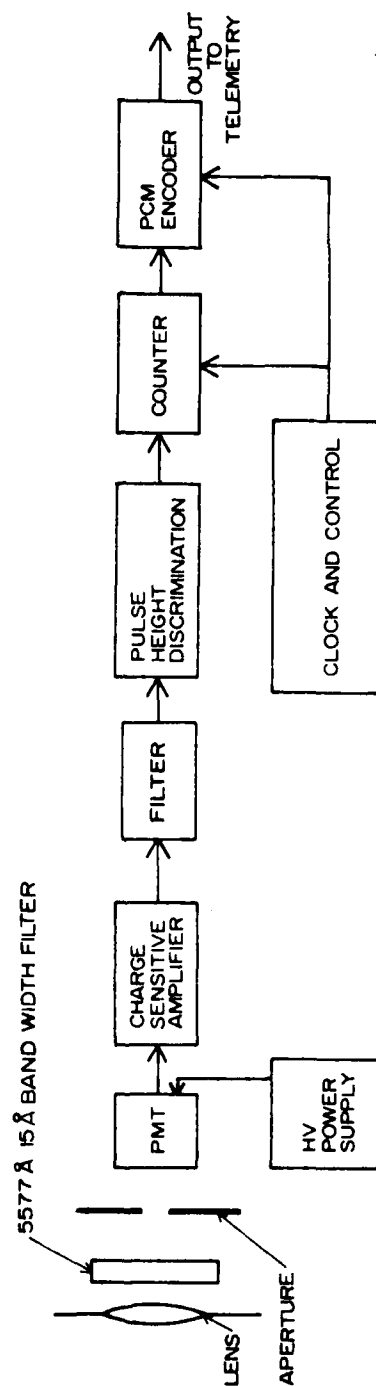


Figure 11. Block Diagram of [O1]  $\lambda 5577\text{\AA}$  Photometer.

## PERFORMANCE OF EBIL SYSTEM

### Electron Gun Performance

The performance of the electron gun is illustrated by the typical results in Figure 12. The gun was operated for about 2.2 min at an  $N_2$  target pressure of  $2.0 \times 10^{-4}$  torr. The cathode-current monitor shows a total variation  $\approx 1\%$  during this period, and indicates a mean cathode current of 67 mA.

An additional check of the electron gun performance was realized from the use of a  $\lambda 3914\text{\AA}$  digital photometer. The photometer was positioned to view the beam in a region  $\approx 18$  inches beyond the magnetic lens assembly. The instrument "viewed" the beam-induced emissions normal to the beam direction with a field-of-view at the beam position significantly larger than the diameter of the beam. Hence, the photometer provided a convenient intensity monitor for the beam emissions. [The stability of the photometer (and associated recording electronics) was found to be  $\approx 1\%$  over time intervals of several minutes. The time constant used to record the information presented in the figure was 0.01 sec.]

The output of the intensity monitor varied by as much as  $\approx 3-4\%$  from the mean during the gun "on" period. Most of this variation is attributed to changes in the target pressure, which was presumably controlled to within  $\pm 2\%$  during this period. The short-term fluctuations in the photometer output exhibit a variation of about  $\pm 1.5\%$ , which is roughly consistent with statistical variations in the counting rate. [mean count rate  $\approx 6.8 \times 10^5 \text{ sec}^{-1}$  and averaging time  $\approx 1.0 \times 10^{-2} \text{ sec} \Rightarrow \approx 6.8 \times 10^3 \text{ counts}$ ;  $(\sqrt{6.8 \times 10^3} / 6.8 \times 10^3) \approx 0.012$ ].

The gun was operated many times under similar conditions yielding results in accord with those presented in the figure. Thus, the stability of the electron-beam source is deemed well within the design specifications.

The magnetic lens used with the modified Pierce-type electron gun provided a fine control of beam geometry, as previously illustrated in Figure 3. Hence, it was conveniently possible to continuously alter the beam geometry in identifying the optimum geometry for light collection by the echelle spectrometer.

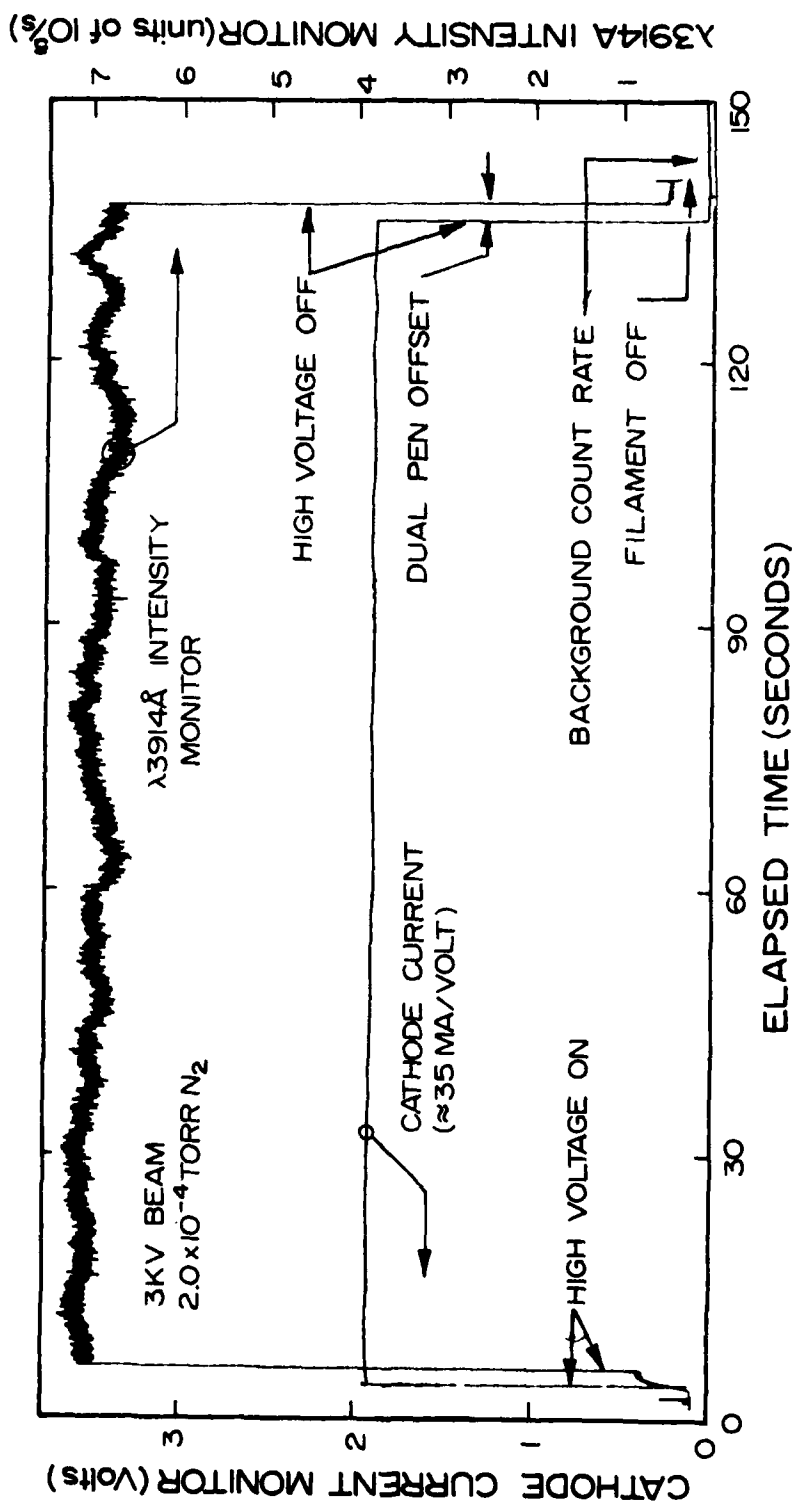


Figure 12. Cathode Current and Intensity Monitor Output vs. Time.



It should be noted that the reading from the cathode current monitor exhibited a distinct pressure dependence. The reading at low pressures consistently suggested a current of about 50 mA. The reading appeared to increase almost linearly with pressure, with a slope of  $\approx 85$  mA/mTorr. The data presented in a subsequent subsection suggest that this increase may actually reflect an increase in beam current, presumably associated with space-charge-neutralization phenomena.

#### Spectral Resolution of the Detection System

The spectral resolution of the EBIL detection system is illustrated in Figure 13. A small neon lamp was used as a light source to yield the spectra in the figure. The intense ArI line at  $\lambda 4259.4\text{\AA}$  appears to be free of spectral contamination and provides a convenient check of the spectral resolution of the instrument in the  $\lambda 4250\text{\AA}$  region. Several checks have consistently yielded an instrument function with a FWHM of about  $1.2\text{\AA}$  (uncertainty  $\approx \pm 0.1\text{\AA}$ ) when using a  $50\text{-}\mu\text{m}$  entrance slit.

#### Vacuum Chamber Tests: Instrument Responsivity

The echelle spectrometer and electron gun system were integrated to form the basic EBIL unit for the rocket-based experiment. Provision was made to mate the EBIL unit to a high vacuum test chamber, as depicted in Figure 14.

A base pressure of  $\approx 10^{-6}$  torr was realized in the  $\approx 50\text{-ft}^3$  vacuum chamber without cooling the optical-baffle cold trap. This background pressure was deemed satisfactory for the preliminary tests. The gas to be used during the test was introduced into the chamber by means of a cold trap and a piezoelectric valve, which was an integral part of an automatic pressure control (APC) system. The feedback signal was provided by a Bayard-Alpert ionization gauge. The APC system is designed to hold the chamber pressure within  $\approx \pm 2\%$  of the selected value.

Initial tests revealed that the field-of-view (FOV) of the echelle spectrometer was canted at a small angle ( $\approx 3^\circ$ ) with respect to the axis of the instrument. This offset prevented the instrument from viewing the beam-induced-emissions in the initial effort. The field-of-view was subsequently mapped and adjustments were made to ensure that the FOV axis intersected the beam axis.

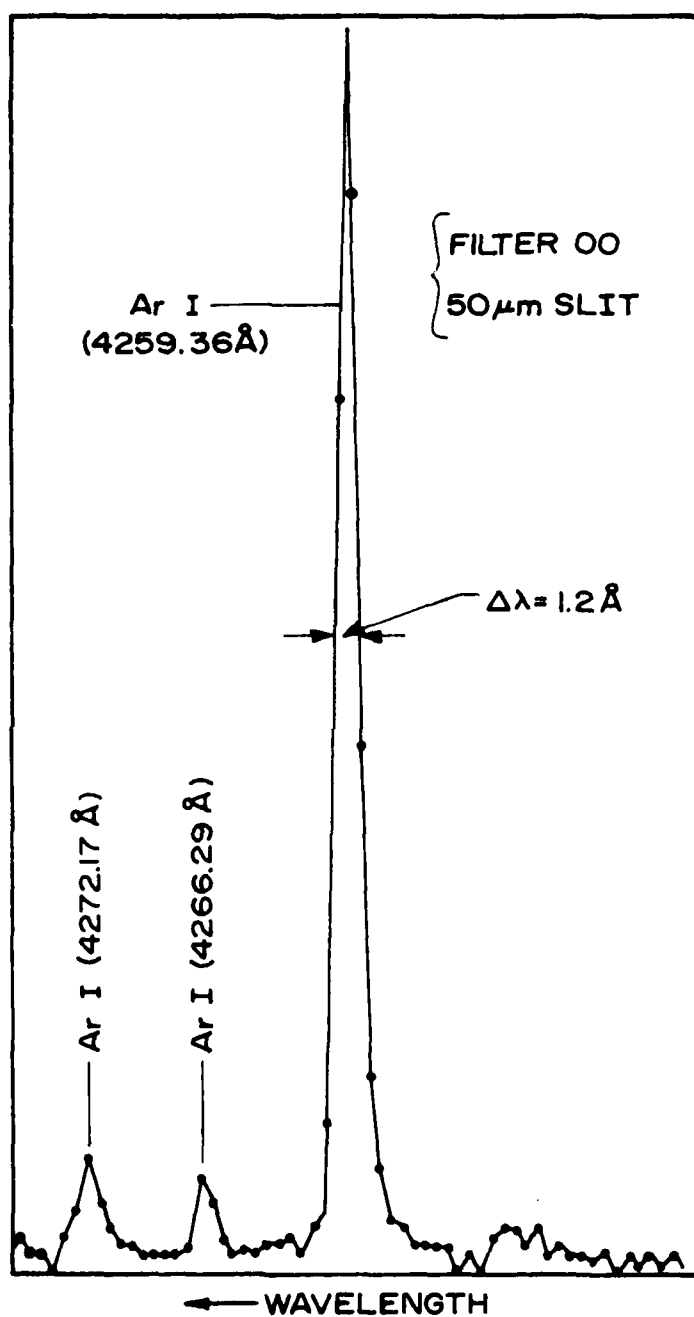


Figure 13. ArI Spectra in the  $\lambda 4250 \text{ Å}$  Region  
Illustrating the Spectral Slit Width of  
the Instrument.

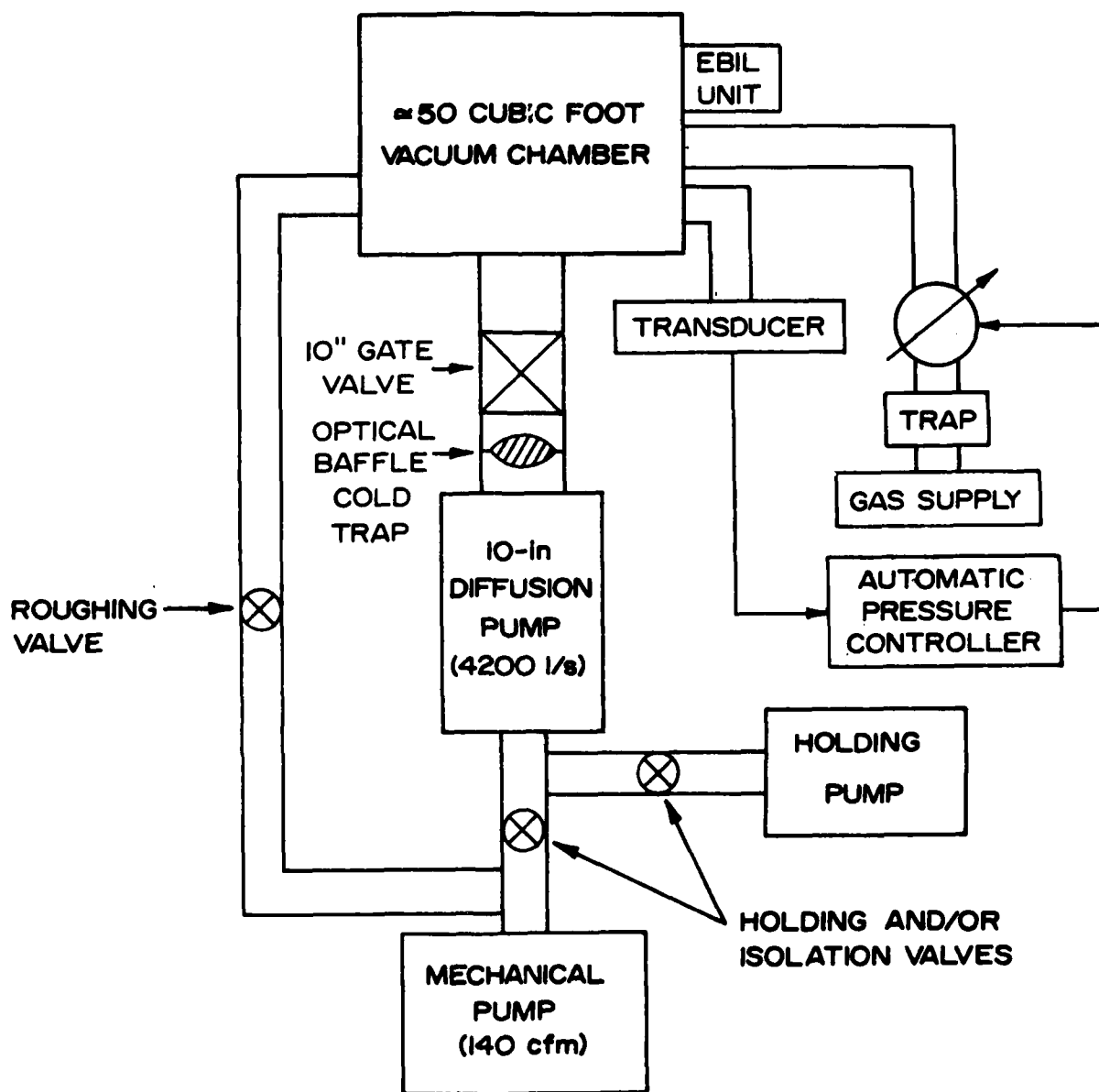


Figure 14. High-Vacuum Test Facility.

The periscope and magnetic lens settings were then adjusted to optimize the response of the spectrometer to the beam-induced emissions. The results depicted in Figure 15 are typical of the spectrometer response when using a 150- $\mu$ m entrance slit. Note that the previously mentioned beam intensity monitor was used during these tests to provide an independent measure of beam-induced emission vs. target pressure.

The response of the instrument has arbitrarily been "keyed" to the R-branch maximum of the  $N_2^+ 1N(0,1)$  band. This procedure is consistent with the use of the (0,1) R-maximum signal to control the "exposure time" for the Reticon. The data reveal that the signal growth rate at the spectral position of the (0,1) R-maximum (ER) depends on the target pressure ( $p \equiv$  ionization gauge reading) in the following approximate manner

$$ER = 0.23p + 0.017p^2, \quad (1)$$

where ER is in V/sec and  $p$  is in units of  $10^{-5}$  torr. The pressure sensitivity in units of  $10^5 \text{ V} \cdot \text{sec}^{-1} \cdot \text{torr}^{-1}$  is thus given by the expression

$$S_p = 0.23 + 0.034p. \quad (2)$$

The linear term in  $S_p$  probably results from the aforementioned dependence of cathode current (and presumably beam current) on target pressure and from the contribution to the observed signal from secondary electrons formed between the anode of the gun and the measurement position. The magnetic field produced by the lens tends to confine the trajectories of many of the secondary electrons to the beam track and hence to accentuate their contribution to the observed signal. (The moderately strong  $N_2$  first positive emissions observed from the region of the beam track close to the viewing region of the echelle spectrometer attests to the plausibility of this assumption.)

It should be noted that the output of the monitor exhibited a pressure dependence which was very nearly identical to that of the spectrometer output. This observation lends additional confidence to the aforementioned interpretation of the pressure dependence of the echelle output.

The implications of these measurements for the proposed thermospheric experiment are presented in a subsequent section of the report.

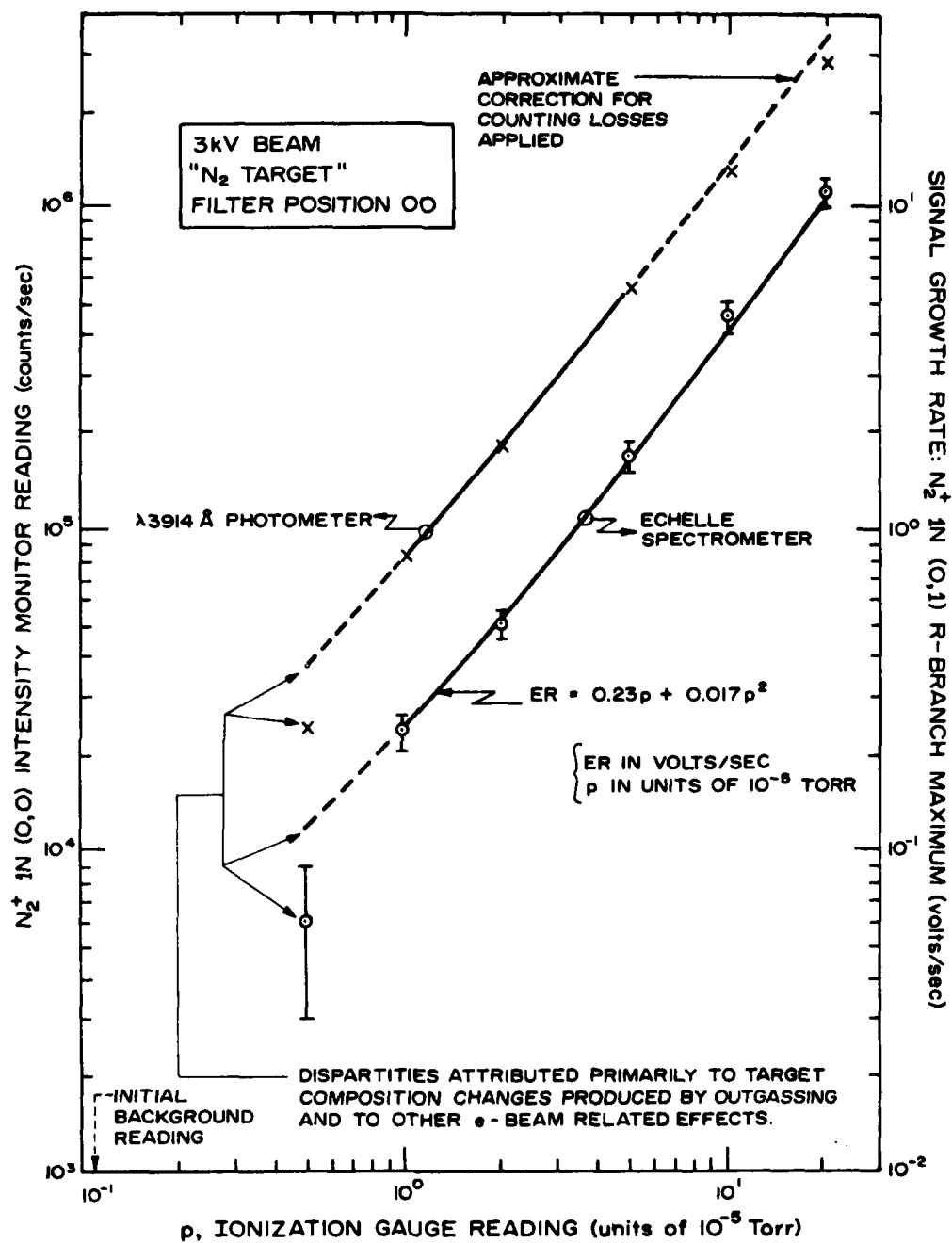


Figure 15. Outputs of Echelle Spectrometer and λ3914Å Intensity Monitor vs. Target Pressure.

### Background and Noise

Background. The *dark signal* of the spectrometer is illustrated for typical operating conditions in Figure 16. This *dark signal* and its attendant noise components will ultimately determine the lower limit for detecting the e-beam-induced atmospheric emissions. The results presented in the figure are considered "typical", but it is important to note that the actual background levels are rather sensitive functions of the effective temperatures of the photodiode array and the image intensifier.

Panel (A) illustrates the background levels with the intensifier off (lower scan) and on (upper scan) for a temperature monitor reading of about 225°K. (Note the "offset" of  $\approx 0.17$  V in interpreting the levels.) The net dark signal with the intensifier "off" is approximately seven tenths of the "on" value. (The noise level can't be reliably determined from the figures owing to the dispersion in the dark-current and sensitivity characteristics of the Reticon elements. Results relating to the noise characteristics of the instrument will be presented in the following subsections.)

Panel (B) of the figure presents *dark signal* results obtained with an opaque mask between the photodiode array and the output screen of the image intensifier. In this case, no perceptible change in dark signal level occurred with the intensifier operating. Hence, the additional "intensifier-on" *dark signal* illustrated in panel (A) is deemed to result from the light produced at the intensifier output by the dark current from the photocathode. This observation appears to be consistent with the estimated intensifier gain together with the equivalent background input (EBI) quoted by the manufacturer.

The *dark signal* from the intensifier-Reticon combination can readily be reduced to  $< 0.5$  V (8-sec integration time) with careful cooling of both components. The dark noise level of the system is presently  $\approx 0.2$  V (peak-to-peak) with the intensifier operating. Hence, further reduction of the *dark signal* level will not greatly affect the dynamic range. [It appears desirable to extend the dynamic range somewhat by carefully identifying and minimizing the noise sources. The practical noise limit appears to be  $\approx 0.05$  V.]

Noise. The *dark noise* level of the instrument has been checked with intensifier on and intensifier off by collecting a large number of output samples from selected Reticon elements. This process has been carried out

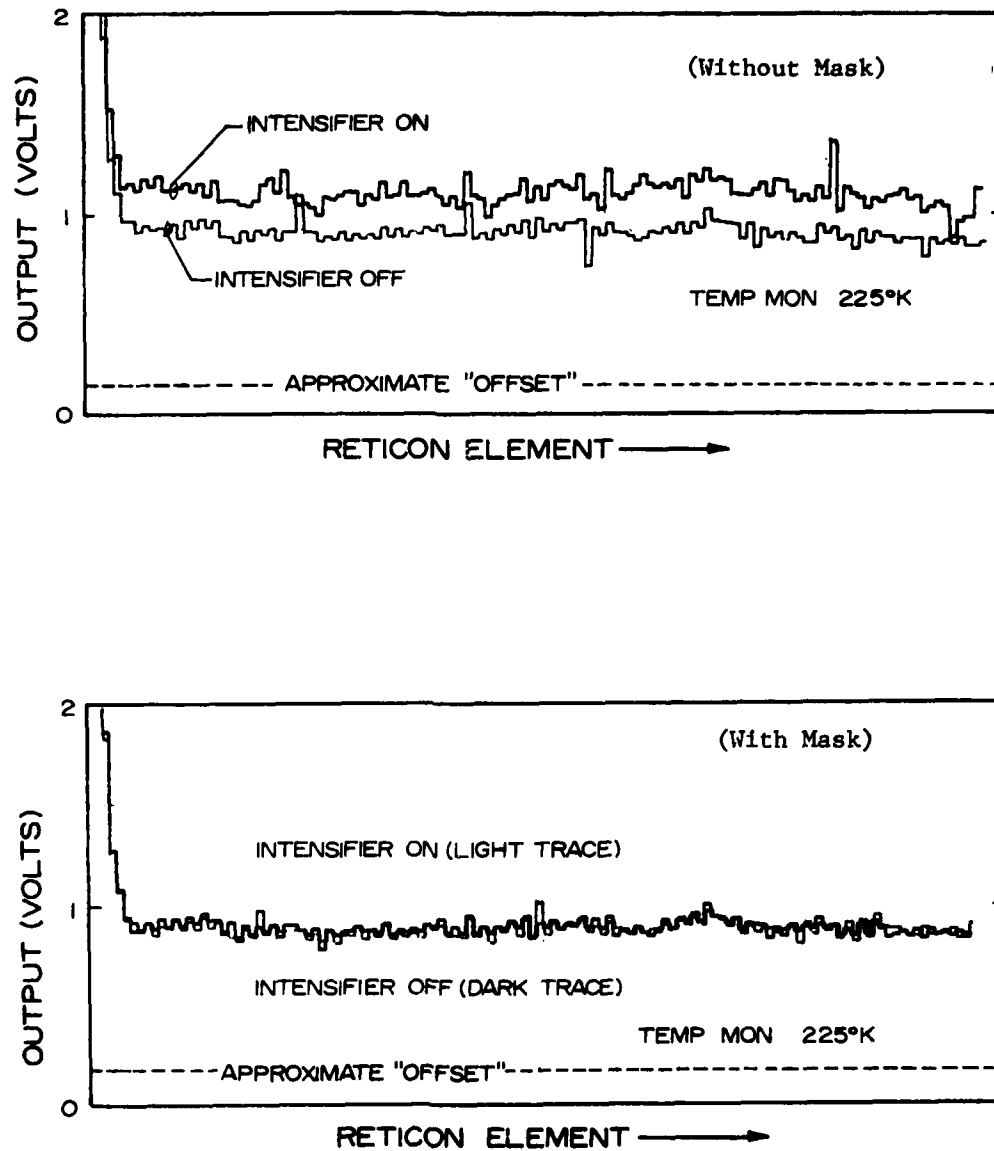


Figure 16. Typical Dark Signal Scans Illustrating Contributions of Reticon and Image Intensifier. Upper Panel: Normal Configuration. Lower Panel: Opaque Mask between Intensifier and Reticon.

both at room temperature and with the photodiode array cooled to a temperature  $\approx 240^\circ\text{K}$ .

With the intensifier off, the standard deviation of the sample population is consistently  $\approx 0.03 - 0.04$  V, essentially independent of the output level. This suggests that the residual, non-periodic, fixed-pattern noise in the Reticon dark level dominates the Reticon noise sources under the present operating conditions.

The extent to which the intensifier contributes to the dark noise level of the system appears to depend on the effective temperatures of both the Reticon and the intensifier. At room temperature (integration time 1 sec) the noise contribution of the intensifier is  $\approx 0.1-0.2$  V p-to-p. The EBI level of the intensifier and its attendant fluctuations are almost negligible under these conditions. However, when the photodiode array is cooled to a temperature  $\approx -40^\circ\text{C}$  (exposure time = 8 sec), the intensifier adds significantly to both the dark signal and the dark noise. Cooling the intensifier photocathode to  $\approx -20^\circ\text{C}$  would probably render this background (and noise) source negligible.

The noise characteristics of the cooled instrument have consistently exceeded design expectations by a large factor when viewing stable, intense light sources. The typical performance relevant to the EBIL experiment is documented in Table 1.

Three sets of 8 exposures each were obtained with the EBIL source operating at an  $\text{N}_2$  target pressure of  $2.0 \times 10^{-4}$  torr. A permanent record of the system response to each exposure was obtained photographically with an oscilloscope and camera. This procedure was dictated by the need to restrict the operating interval for the electron gun, thus requiring a rapid recording of exposures. (The plot-rate capability of the echelle readout unit was inadequate to permit convenient collection of the data by this means.) Hence, a photographic method was adopted which permitted the acquisition of 8 exposures (one Polaroid film-pack) in slightly over one minute. An intensity monitor was used to assess the contribution of source intensity changes to the observed amplitude dispersion. Relative source intensities were noted when exposures were taken, as indicated in the table.



TABLE 1. Amplitude dispersion of the  $N_2^+ \text{IN}(1,2)$  P-branch maximum. (Source pressure:  $2.0 \times 10^{-4}$  torr; 150- $\mu$ m entrance slit; 1-sec integration time.)

SET NO.	1		2		3	
EXPOSURE NO.	(1,2) P-Max. Amplitude	Intensity Mon. (relative)	(1,2) P-Max. Amplitude	Intensity Mon. (relative)	(1,2) P-Max. Amplitude	Intensity Mon. (relative)
1	2.65	1.00	3.00	1.02	2.40	1.00
2	2.80	1.00	2.20	1.01	2.30	1.00
3	2.20	1.02	2.70	0.99	2.20	1.00
4	2.75	1.01	2.60	1.02	2.30	1.00
5	2.05	1.01	2.35	1.01	2.60	0.99
6	2.60	1.01	2.05	1.00	2.40	1.00
7	2.30	1.03	2.25	1.01	2.50	0.98
8	2.80	1.02	3.05	1.01	3.00	1.00
MEAN	2.52		2.53		2.46	
S.D.	0.29		0.37		0.25	

The  $N_2^+1N(1,2)P_{\max}$  amplitudes were carefully read from the permanent data records with an estimated uncertainty of  $\approx \pm 2.5\%$ . The dispersion in the readings of the intensity monitor is closer to  $\pm 1\%$ . Hence, the  $\approx \pm 10-15\%$  dispersion in the  $P_{\max}$  amplitudes is deemed a fairly representative measure of the system performance. An examination of the  $(0,1) R_{\max}$  region yields a comparable percentage spread of amplitudes ( $\approx \pm 0.5 V$  about a mean of  $\approx 4.5 V$  or  $\approx \pm 10\%$ ).

# IMPLICATION OF RESULTS FOR PROPOSED MEASUREMENTS

The implication of the results presented in the previous section are summarized in Figures 17 and 18. The vacuum chamber measurements of instrument responsivity to the beam-induced emissions have been combined with  $N_2$  densities from the CIRA 1965 atmospheric model to yield the predicted  $N_2^+1N(0,1) P_{\max}$  signal growth rate vs. altitude displayed in Figure 17. It is seen that the  $N_2^+1N(0,1) P_{\max}$  signal is predicted to approach the system *dark signal* at an altitude of roughly 130 km. A seemingly conservative figure was adopted for the *dark signal*. Careful cooling of the instrument should reduce the *dark signal* rate to somewhat less than 0.1 V/sec.

The lower limit shown in the figure reflects the dark noise level of the instrument. In preparing the figure, a value of 0.17 V was assigned to this noise source. This value is consistent with a quick-look evaluation, but a more definitive check should be made.

The basic noise limitation for the present type of system is reflected in the residual, non-periodic, fixed-pattern noise component in the dark level of the Reticon. As previously mentioned, this component appears to be  $\approx \pm(0.03-0.04)$  V. Hence, the dark noise performance of the present system is significantly poorer than this limiting value. The noise level can undoubtedly be reduced below the present figure through a systematic effort toward this end. Hence, instrument sensitivity extending to altitudes of  $\approx 150$  km is deemed a possibility if careful attention is given to the minimization of noise sources.

The observed fluctuations of the order  $\pm 10\%$  in the  $N_2^+1N$  signal levels may be compared in Figure 15 with the expected departure of the (0,1)/(1,2) intensity ratio from the "cool" value for selected values of  $T_v(N_2)$ . It is difficult to reliably translate the single-element dispersion into a true confidence level for a band intensity based on a large number of spectral elements. The use of synthetic spectra and a least-squares, curve-fitting approach would undoubtedly decrease the uncertainty, but until the behavior

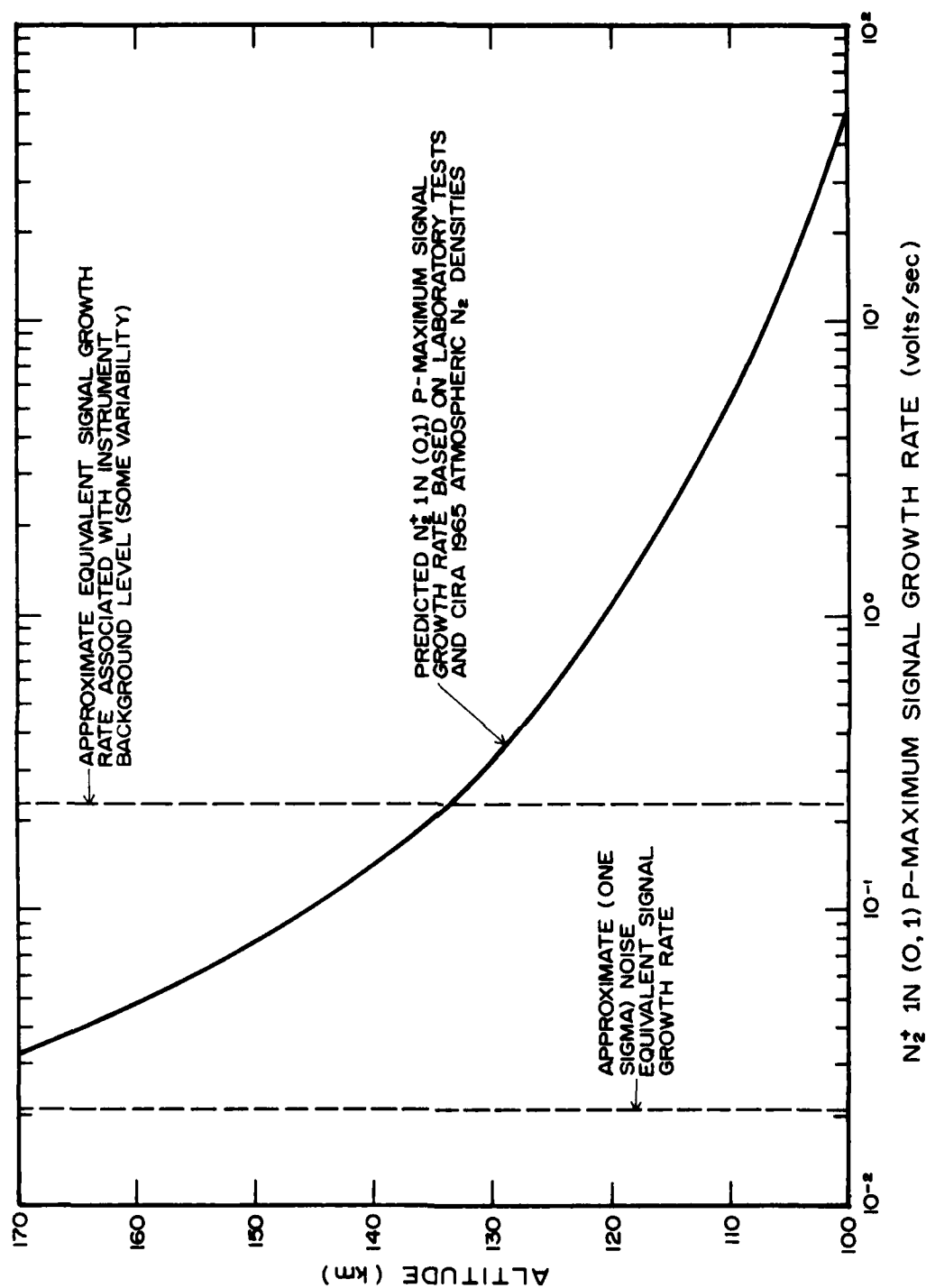


Figure 17. Predicted  $N_2 1N (0,1) P_{\max}$  Signal Growth Rate vs. Altitude.

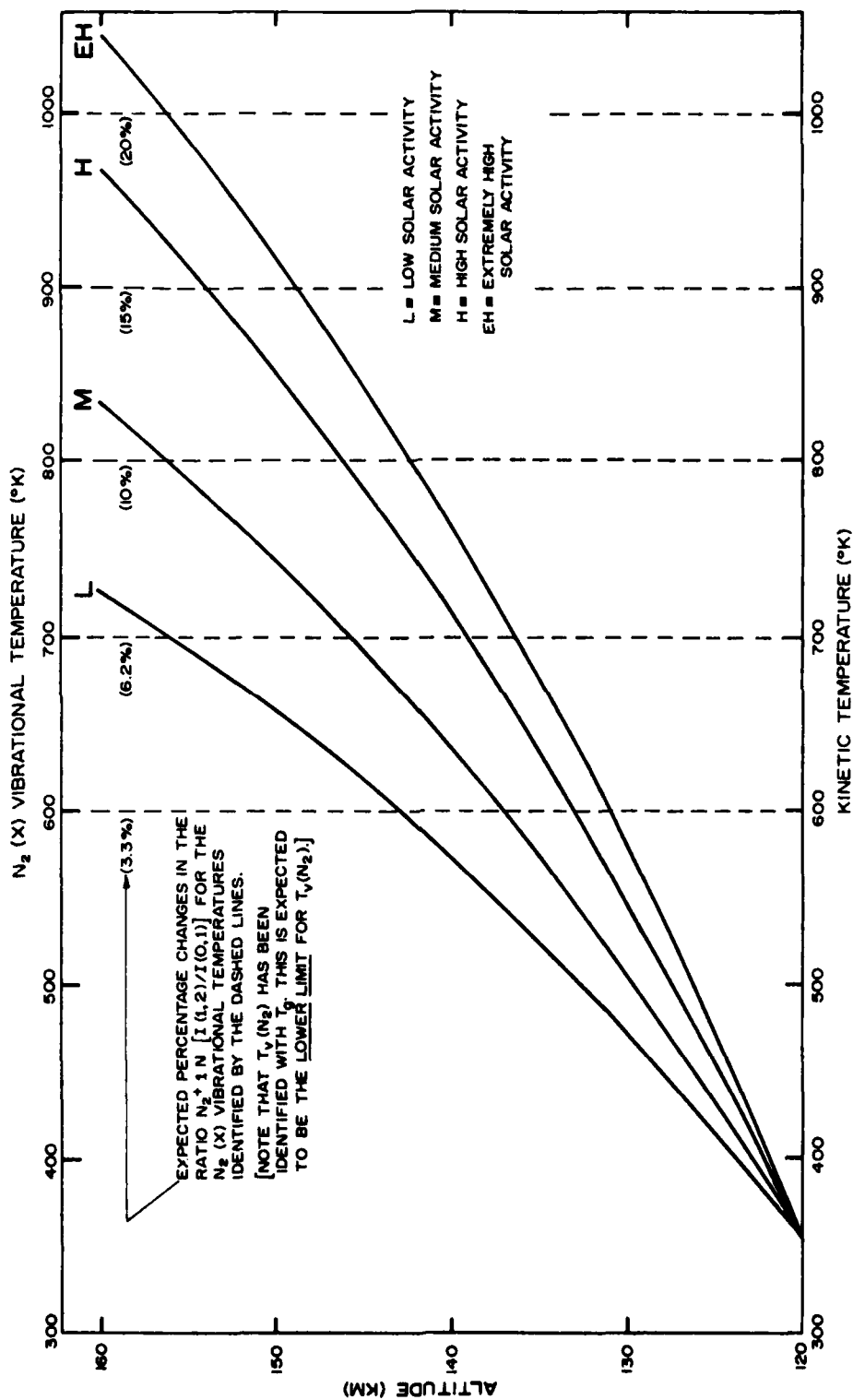


Figure 18. Illustration of Expected Changes in  $N_2^+ 1N [I(1,2)/I(0,1)]$  with  $T_v(N_2)$ : Correlation with Height-Temperature Profiles for Various Levels of Solar Activity.

of the system noise is investigated in more depth, a reliable estimate of the improvement can't be made.

In order to facilitate an evaluation of the implications of system performance, atmospheric kinetic temperature profiles have been included in Figure 19 for several levels of solar activity. Assuming  $T_v(N_2) = T_g$ , it is seen that  $[I(1,2)/I(0,1)]$  is expected to depart from the "cool" ratio by 10-15% at an altitude of 150 km in the case of high solar activity and by slightly more than 15% in the case of extremely high solar activity. At altitudes of  $\leq 140$  km, the expected departure from the "cool" ratio is  $< 10\%$  even for the EH model. Hence, it seems unlikely that significant  $T_v(N_2)$  results can be realized at altitudes  $\leq 140$  km without major modification and improvement of the EBIL system. However, optimization of the S/N performance of the present system may permit the measurement of  $T_v(N_2)$  in the vicinity of 150 km.

The diurnal variation of atmospheric temperatures together with the apparent need to optimize the measurement conditions suggests the desirability of an early evening flight. Figure 19 presents diurnal temperature variations at altitudes of 140, 150, and 160 km for the high-solar-activity model. The kinetic temperature is expected to be  $\approx 850^\circ\text{K}$  at 150 km in the early evening, according to the model.

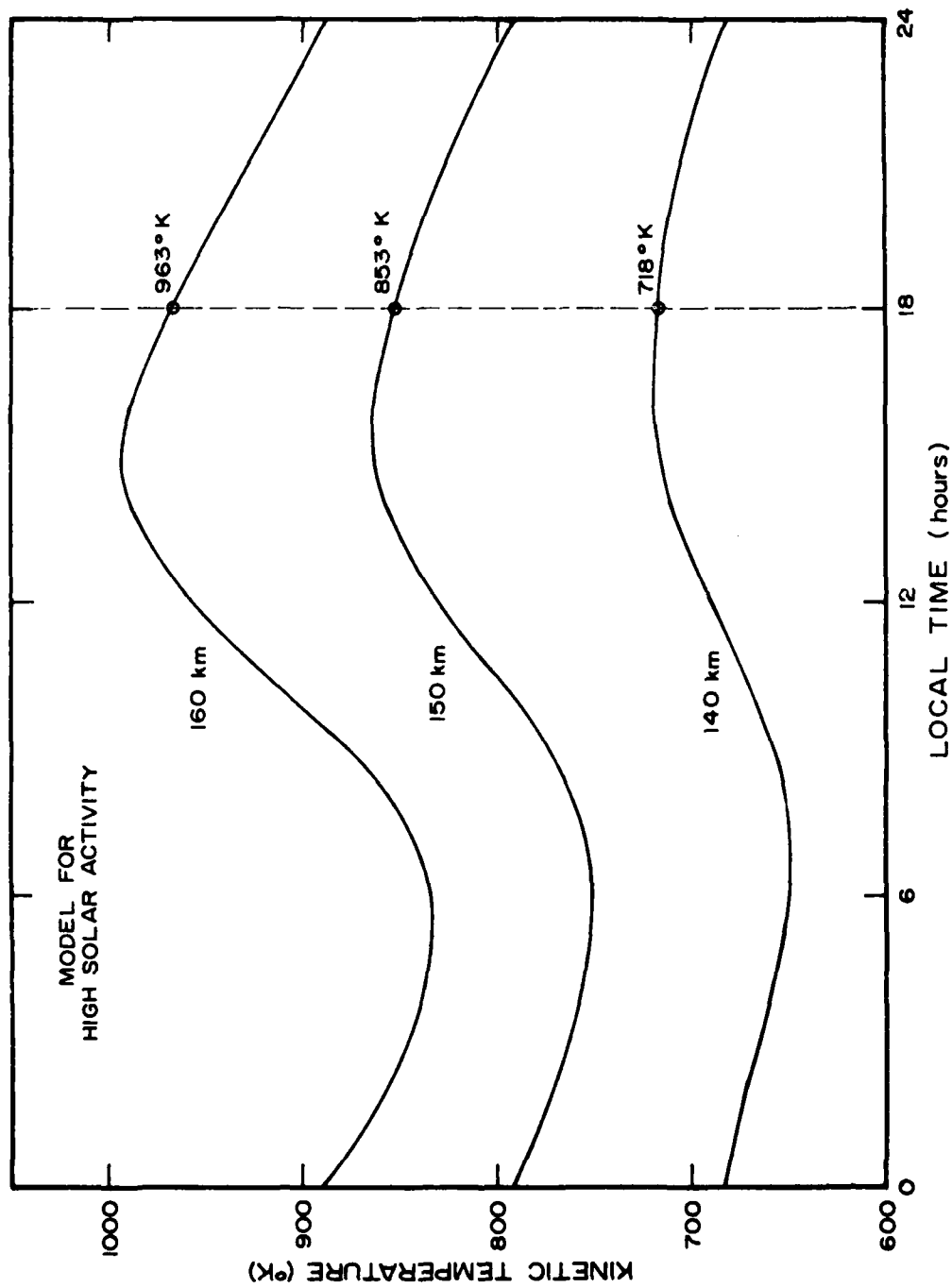


Figure 19. Diurnal Variation of Atmospheric Temperatures at 140, 150, and 160 km During a Period of High Solar Activity.

## SUMMARY

An electron gun system which meets the design specifications has been built and tested. The unit provides a well-focused,  $>50\text{-mA}$  beam at 3 kV. The gun unit was integrated with the government-furnished echelle spectrometer, and an evaluation of system performance was carried out. The performance checks revealed the need for additional effort to optimize system performance. The system component which appears to limit signal-to-noise performance is the image intensifier.

In addition, a resonance fluorescence system for [0] measurements was developed together with a related [01]  $\lambda 5577\text{\AA}$  photometer.



## RECOMMENDATIONS

It is suggested that the S/N performance of the system be optimized. This will entail a careful evaluation and optimization of the image intensifier. Factors which should be considered include: (i) optimum gain setting, (ii) possible cooling to reduce the EBI, and (iii) reduction of the converter-associated noise in the output of the Reticon.

A significant improvement in system performance could be realized by using an S-series Reticon. However, this would entail a significant alteration of the present system. The possibility of implementing this approach should be fully explored.

## REFERENCES

- Breig, E.L., M.E. Brennan, and R.J. McNeal, *J. Geophys. Res.* 78:1225, 1973.
- Hansen, D.F., M.P. Shuler, Jr., and A.H. Tuttle, Final Report by H.S.S. Inc., Bedford, Massachusetts, to Air Force Geophysics Laboratories (OPR) under Contract F19628-76-C-0199, 1 September 1978.
- Howlett, L.C., W.R. Pendleton Jr., and A.J. Shaw, Mesospheric and Lower Thermospheric Atomic Oxygen Measurements, *EOS, Trans. Am. Geophys. U.*, 60:899, 13 November 1979.
- Kumer, J.B., in *Atmospheres of Earth and the Planets*, B.M. McCormac (Ed.), D. Reidel Publishing Co., Dordrecht, Holland, pp. 347-358, 1975.
- Kummler, R.H. and M.H. Bortner, *Space Research XII*, p. 711, 1972.
- Newton, G.P., J.G. Walker and P.H.E. Meijer, *Trans. Am. Geophys. U.*, 54: 402, 1973.
- O'Neil, R.R., W.R. Pendleton, Jr., A.M. Hart and A.T. Stair, Jr., *J. Geophys. Res.*, 79:1942, 1974.
- Pierce, J.R., *J. Appl. Phys.*, 11:548, 1940.
- Pierce, J.R., *Theory and Design of Electron Beams*, Van Nostrand, Princeton, New Jersey, 1949.
- Stair, A.T. Jr., J.C. Ulwick, K.D. Baker and D.J. Baker, in *Atmospheres of Earth and the Planets*, B.M. McCormac (ed.), D. Reidel Publishing Co., Dordrecht, Holland, pp. 335-346, 1975.
- Schunk, R.W. and P.M. Banks, *Geophys. Res. L.*, 2(6):239, 1975.
- Strobel, D.F. and M.B. McElroy, *Plan. Space Sci.*, 18:1181, 1970.
- Torr, D.G. and W.E. Sharp, *Geophys. Res. L.*, 6:860, 1979.
- Vallance Jones, A., *Aurora*, D. Reidel Publishing Co., Dordrecht, Holland, 1974.

## APPENDICES

APPENDIX A

COPY OF ELECTRON GUN  
DESIGN EVALUATION

## TABLE OF CONTENTS

FOREWORD . . . . .	52
INTRODUCTION . . . . .	53
BASIC DESIGN CONSIDERATIONS . . . . .	53
Electron Gun Perveance . . . . .	53
Operating Point: Optimum Excitation Rate .	54
Beam Geometry . . . . .	56
Beam Stability . . . . .	59
PROPOSED GUN DESIGN . . . . .	59
SUMMARY AND CONCLUSIONS . . . . .	63
REFERENCES . . . . .	63
ATTACHMENT A . . . . .	64

## FOREWORD

The present design evaluation report is submitted in response to the data requirements under Contract No. F19628-78-C-0103. The report addresses Sub-Line Item 0001AA of Line Item 0001, the study of design options for a rocket-borne electron source. The design evaluation is limited to the basic electron-beam source and the associated control unit. The consideration of other payload subsystems will be restricted to their impact on the electron-source design.

## INTRODUCTION

The design evaluation presented in this report focuses on the identification of an "optimum" electron beam source for use in a rocket based electron-beam-induced-luminescence (EBIL) system. Mechanical, electrical and optical constraints imposed by a government-furnished rocket spectrometer and an Astrobee F test vehicle have largely been identified through earlier interactions with cognizant individuals. The specifications delineated in Sub-Line Item 0001AA of the schedule under Contract F19628-78-C-0103 have been considered together with these constraints in the design evaluation. A list of the design requirements, as outlined in the contract, is provided in Attachment A.

Progress has been made in designing and developing a prototype electron gun consistent with the "optimum" design. The detailing of this effort might more appropriately be included in the initial quarterly status report. However, we have chosen to include a description of the prototype electron gun design following a presentation of the design analysis.

## BASIC DESIGN CONSIDERATIONS

### Electron Gun Perveance

It is convenient to classify electron guns (and beams) in terms of a parameter called "the perveance," defined as the ratio of the beam current ( $I_0$ ) to the three-halves power of the accelerating voltage ( $V_0$ ). In the rationalized MKS system, the unit of perveance is  $[I_0/V_0^{3/2}] \equiv \text{amp volt}^{-3/2} \equiv \text{perv}$ . The submultiple  $\mu\text{perv}$  ( $\equiv 10^{-6} \text{ perv}$ ) is convenient for characterizing electron guns of interest to the present design criteria. For example, an electron gun which yields a 3 kV, 50-mA beam is characterized by a perveance of 0.3  $\mu\text{perv}$ .

The design of electron guns to produce electron beams of very low perveance ( $\sim 10^{-9}$  or 0.001  $\mu\text{perv}$ ) can usually be made without considering the effects of space charge in the gun. (This situation is typified by

the electron gun in a conventional cathode-ray tube.) However, space-charge forces are of predominant importance in electron guns characterized by perveance values  $\lesssim 0.1 \mu\text{perv}$ . It is seen that this range encompasses those guns of interest to the present design evaluation.

The perveance of convergent, solid-beam electron guns of *good optical quality* is limited to  $\lesssim 3 \mu\text{perv}$ , but a considerable amount of empirical effort is generally required to produce such guns with perveance values in the range  $\approx 1-3 \mu\text{perv}$ . Electron guns in the intermediate perveance range ( $\approx 0.1 - 0.8 \mu\text{perv}$ ) are designed by a straightforward extension of the Pierce technique. [See, e.g., *Brewer* (1967).]

A perveance of  $\geq 1 \mu\text{perv}$  would seem a realistic goal which is compatible with the design requirements. An electron gun characterized by a perveance value of  $1.0 \mu\text{perv}$  should yield a 160-mA beam at an operating voltage of 3 kV. The beam power level for such a gun would be  $\approx 0.5 \text{ kW}$ . The associated payload appears well within the constraints imposed by the test vehicle performance capability and the desired apogee. Indeed, the use of ballast will be required to limit the flight apogee to  $\approx 180 \text{ km}$  with the anticipated payload.

#### Operating Point: Optimum Excitation Rate

Consider the following general experimental situation in which a pure gaseous target (number density  $n$ ) is bombarded with a nearly mono-energetic beam of electrons (current density  $j$ , energy  $E$ ) resulting in the formation of excited species. Denote the excitation cross section for producing excited species in a certain level  $k$  by  $\sigma_{gk}(E)$ , where  $gk$  signifies excitation from the ground level  $g$  to the excited level  $k$ . The volume production rate of excited species in level  $k$  due to the excitation by primary electrons is then given by

$$P_k = (j/e) n \sigma_{gk} \quad (1)$$

It is assumed that single-collision conditions pertain and cascade to level  $k$  from higher levels may be neglected. Hence, Equation 1 represents the total volume production rate for species in level  $k$ .



The ratio  $(P_k/n) \equiv R_k$  provides a measure of the effectiveness of the beam electrons in producing the excited species of interest. The quantities  $j$  and  $\sigma_{gk}$  both depend on the energy  $E$  of the incident particles in most experimental situations. Thus it is convenient to examine the energy dependence of the product  $j(E) \sigma_{gk}(E)$  in seeking an optimum excitation rate.

The energy dependence of the excitation cross section for the process of primary interest, i.e.,  $e + N_2(X^1\Sigma_g^+, v) \rightarrow 2e + N_2^+(B^2\Sigma_u^+, v')$ , is known to closely follow the Bethe-Born approximation for  $E > 70$  eV (Borst and Zipf, 1970; Pendleton and Weaver, 1978). For nonrelativistic energies ( $E \ll 0.51$  MeV), the excitation cross section may be written in the form

$$\sigma_{gk}(E) = (A/E) \ln(BE), \quad (2)$$

where  $A$  and  $B$  are constants and  $80 \text{ eV} \leq E \ll 0.51 \text{ MeV}$ .

The energy dependence of the current density is assumed to follow "Child's law", i.e., the three-halves power dependence which typifies true space-charge-limited operation. Hence, the expression for  $j$  becomes

$$j(E) = KE^{\frac{3}{2}}, \quad (3)$$

where  $K$  is a constant, and the energy dependence of  $R_k(E)$  is given by

$$R_k(E) = CE^{\frac{1}{2}} \ln(BE), \quad (4)$$

where  $C$  is a constant.

This result suggests that the beam energy  $E$  should be made very large if the full effectiveness of the source is to be realized. However, practical design limitations are normally set by considerations relating to electrical breakdown and to the requisite power supply. The energy dependence of the relative effective excitation rate is given in Table 1, together with the beam power, for a 1.0- $\mu$ perv electron gun.

Table A1. Relative excitation rate  $R_k$  and beam power  $P$  vs. energy  $E$  for a 1.0- $\mu$ perv electron gun.

$E$ (keV)	$R_k^a$ (relative)	$P$ (kW)
0.10	0.04	----
0.30	0.15	0.0016
1.0	0.43	0.032
3.0	1.0 <sup>b</sup>	0.49
10	2.3	10
30	4.9	160

<sup>a</sup>See text for definition and pertinent assumptions.

<sup>b</sup>Point of normalization (preliminary design value for  $E$ )

The figures in column 3 of Table 1 reflect the relatively rapid increase in beam power with increasing accelerating voltage. The beam power is proportional to the (5/2)-power of the accelerating voltage under the assumed conditions, and the power-supply demands become excessive for a 1.0- $\mu$ perv gun operating at voltages  $> 10$  kV.

#### Beam Geometry

The beam geometry becomes an important design factor in the experiment of interest owing primarily to the field-of-view characteristics of the echelle spectrometer (Hansen & Shuler, 1976). A beam diameter  $\approx 1$  cm at a distance of roughly 20 cm from the anode of the gun is adopted for a design goal. It appears possible to realize a beam approaching the desired geometric characteristics with a 1-2  $\mu$ perv gun based on the modified Pierce design. However, the electron-optical characteristics of such guns are difficult to calculate, and recourse to a semiempirical approach is usually dictated.

The emergent beam from a focused design Pierce-type gun passes through a minimum beam diameter at a calculable distance from the anode of the gun, the distance depending on several gun parameters. The ratio of minimum beam diameter to the initial diameter at the anode of the gun can also be computed for Pierce guns. These distances become much less certain for the modified-Pierce guns since the design is semiempirical.

The electron trajectories outside the gun are strongly affected by beam space charge forces for moderate-to-high perveance guns. Hence, under the assumption that these forces control the behavior of the beam geometry in the region beyond the "cross-over point" (minimum beam radius), the beam should spread in a manner consistent with the "universal" beam-envelope curve (Spangenberg, 1948). The expected spreading characteristics of a 1.0- $\mu$ perv beam of 1.0-cm minimum diameter is given in Table 2.

Table A2. Space-charge spreading of an initially parallel-flow electron beam.\*

distance (cm)	beam diameter (cm)
0	1.0
5	1.3
10	1.8
15	2.6
20	3.5
25	4.6
30	5.7
35	6.8
40	8.1

\* Assumptions:

- (1) Perveance = 1.0  $\mu$ perv
- (2) No Space Charge Neutralization
- (3) Initial Beam Diameter = 1.0 cm

The relatively rapid spreading of an initially convergent 1.0- $\mu$ perv electron beam in the region beyond the cross-over point is illustrated in the table. The beam is expected to expand to twice the initial diameter  $D_0$  in a distance  $\approx 12 D_0$  when beam space charge dominates.

In practice, it is found that the spreading is frequently less than the predicted value, even though the predicted current and voltage dependence is obeyed. The reduction in spreading apparently stems from partial neutralization of the negative beam space charge by positive ions formed in the beam region through collisions of the primary electrons with residual gas atoms and molecules. Hence, the universal space-charge spreading illustrated in Table 2 for a 1.0- $\mu$ perv beam should represent worst-case conditions.

A minimum beam diameter of  $\approx 0.75$  cm at a distance of  $\approx 18$  cm from the anode of the gun would match the field-of-view characteristics of the spectrometer. However, an element of risk is incurred if this is done since relatively small beam displacements could produce large changes in the collection of beam-induced emissions. An alternate procedure is to overfill the field of view by a significant factor. This approach would reduce the impact of beam displacement on the output of the spectrometer but would also compromise the signal level by a factor of roughly  $(d/D)^2$  where  $d$  is the pertinent field-of-view dimension,  $D$  is the beam diameter in the primary observation region, and  $d < D$ . If  $(D/d) \approx 2$  is deemed a satisfactory relationship, then  $D \approx 1.5$  cm appears consistent with the foreoptics design of the spectrometer.

It is anticipated that the beam axis will be antiparallel to the  $\vec{B}$  field of the earth to within roughly  $5^\circ$  ( $3^\circ$  - ACS;  $2^\circ$  - MECHANICAL) during the data-taking portion of the flight. A misalignment will cause the beam electrons to follow a helical path after exiting the gun. The radius  $\rho$  of the helix is given by

$$\rho = (mv \sin\theta / eB),$$

where  $v$  is the speed of an electron after exiting the gun and  $\theta$  is the angle between the velocity vector and  $\vec{B}$ . Assuming the set of values ( $v = 3.3 \times 10^7$  m/sec;  $\theta = 5.0^\circ$ ;  $B = 6.0 \times 10^{-5}$  weber/m<sup>2</sup>), one obtains

a radius of 0.27 m or 27 cm. However, the electron flight time to the observation region is small compared to the reciprocal of the cyclotron frequency. Hence, the anticipated maximum beam deflection at the observation region is much smaller than this figure.

### Beam Stability

The effective energy of the beam electrons must be well stabilized or accurately monitored in the case of species concentration measurements. The effective energy used during the calibration phase should be maintained during the flight if cross-section-related corrections are to be avoided. The primary impact of changes in accelerating voltage is expected to be cross-section related since the beam geometry for the proposed source is largely independent of the accelerating voltage.

The high voltage supply will be stabilized in the flight unit. In principle, this should also stabilize the beam current. However, changes in the space-charge conditions owing to the presence of positive ions could affect both the beam current and the space-charge spreading of the beam. Attention will be given to these effects during the developmental phase since reliable computations are deemed impractical.

### PROPOSED GUN DESIGN

A consideration of electron guns which satisfy the design criteria reveals the modified-Pierce type to be potentially the most suitable for the present application. These guns are typically simple, self-focused, rugged, and reasonably compatible with the use of an oxidation-resistant, directly-heated electron source (filament of tungsten or a tungsten alloy). The last feature permits an open structure to be flown, thus simplifying the flight operations and thereby increasing the probability of a successful experiment.

Two features of the proposed gun design which render impossible a straightforward calculation of the anticipated performance characteristics are: (i) a high perveance and (ii) a flat, bifilar spiral filament. The

design problems which are introduced by these features will subsequently be clarified in terms of perturbations on the basic Pierce design described below. Some general guidelines for treating the perturbations emerge from a consideration of the Pierce design, but a semiempirical method of solution is dictated by the computational complexity.

An illustration of a simplified Pierce-type configuration is presented in Figure 1 in order to clarify pertinent design notation. In practice the cathode electrode and the anode must be shaped to compensate for the departure from the geometry assumed in treating space-charge-limited flow between concentric spheres. No attempt has been made in the figure to indicate the shaping of the electrodes. The symbols used in the figure are identified in Table 3.

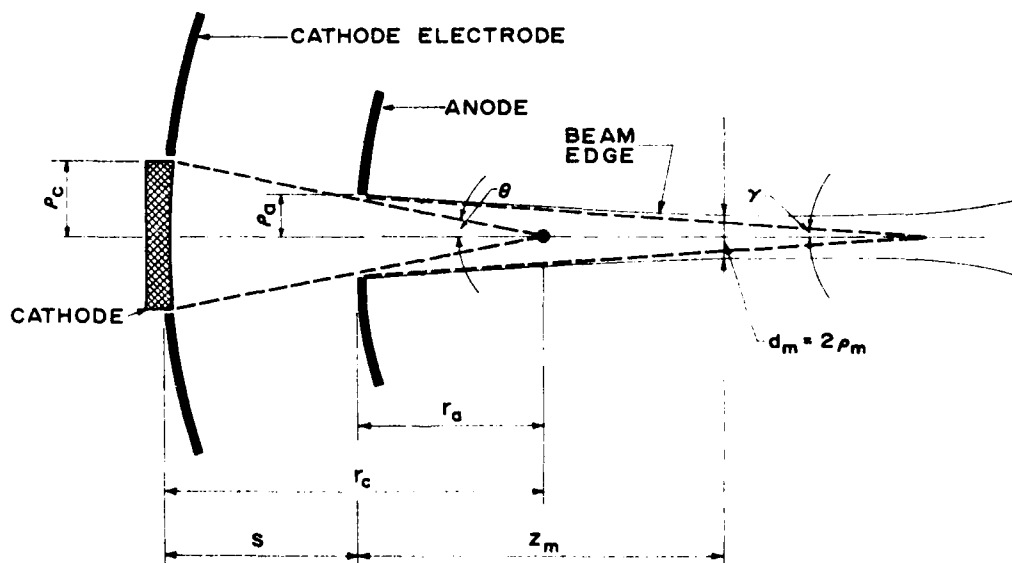


Figure 1A. Illustration of notation employed in the analysis of an idealized spherical flow Pierce-type electron gun. Note that no attempt has been made to illustrate the required shaping of the electrodes.

Table A3. Identification of symbols used in Figure 1A

Symbol	Identification
$\rho_c$	radius of cathode (cylindrical coordinates)
$\rho_a$	radius of anode aperture ( " " )
$\rho_m(d_m)$	minimum beam radius (diameter) ( " " )
$r_c$	radius of cathode (spherical coordinates)
$r_a$	radius of anode ( " " )
$s$	cathode - anode separation
$z_m$	distance from anode aperture to beam minimum
$\theta$	semiangle of the beam between cathode and aperture
$\gamma$	semiangle of the beam leaving the aperture

The general configuration illustrated in Figure 1 was proposed by Pierce (1940) as a potentially significant method for producing a uniformly convergent electron beam. A theory and design philosophy evolved (Pierce, 1940, 1949) which has formed the basis, with some modification, of nearly all high-density guns built in recent years. It will suffice for present purposes to summarize design considerations for the idealized Pierce gun and to note the problems which result from the previously-mentioned design considerations (high perveance and flat filamentary-type source). The Pierce design equations are expected to apply to the present design as a zeroth-order approximation. It is anticipated that empirical modifications of the Pierce design will be required to obtain the desired performance.

The perveance of the idealized electron gun can be estimated from the design equation

$$(I/V^{\frac{3}{2}}) = \{29.34[\sin^2(\theta/2)]/(-\alpha)^2\} \mu\text{perv}$$

by selecting an initial beam convergence angle  $\theta$  and a value for the ratio  $(r_a/r_c)$ . The parameter  $\alpha$  is the spherical space-charge-limited current factor (Langmuir & Blodgett, 1924) given by the series

$$\alpha = \sum_{i=1}^{\infty} (-1)^{i+1} c_i \beta^i$$

where the leading constants ( $c_1, \dots, c_4$ ) have numerical values (1; 0.30; 0.75; 0.0014) and  $\beta = \ln(r_a/r_c)$ . Preliminary design values of  $\theta = 15^\circ$  and  $(r_c/r_a) \approx 1.57$  yield a perveance estimate of 1.8  $\mu\text{perv}$ . However, it must be cautioned that this figure neglects anode-aperture and plane-emitter effects.

The presence of the anode aperture poses significant design problems when the ratio  $(2\rho_a/s)$  approaches unity. It follows from the geometry of Figure 1 that  $(2\rho_a/s) = (2 \sin \theta)(r_a/r_c)[1 - (r_a/r_c)]^{-1} \approx 0.91$  for the preliminary design. Hence, some empirical "tuning" of electrode shapes is anticipated in order for the gun perveance to approach the zeroth-order estimate. Experience has shown that the relatively large apertures normally required to realize a high perveance tend to produce a low current efficiency and poor focal properties. The low current efficiency (ratio of actual beam current outside gun to cathode emission current) implies that a significant fraction of the cathode emission current has been lost to the anode structure.

The planar filamentary-type source represents a departure from the Pierce geometry and is expected to influence the shape of the beam-forming electrodes in the final design. (An additional point relating to the filamentary-type source merits attention. A tungsten filament becomes brittle upon temperature cycling under normal conditions. Hence, it is imperative that cycled filaments be given severe shake tests in order to clarify the possibility of using a single filament in the calibration, launch-site checks, and the actual flight experiment.)

The minimum radius of the beam,  $\rho_m$ , expected on the basis of the idealized Pierce design can also be predicted from the equation

$$(\rho_m/\rho_c) = (r_a/r_c) \exp \left[ -(\tan \gamma / 174\sqrt{P})^2 \right],$$

where  $P$  is the perveance of the gun. The exponential is approximately unity for the case of interest, and the theoretical minimum radius of the beam is found to be  $\approx 0.6 \rho_c$ . The axial distance from the anode to the



beam minimum can also be estimated from the simplified theory and is found to be  $\approx 0.3 r_c$  for the design parameters. Hence, the beam should be nearly parallel when it emerges from the anode of the gun.

#### SUMMARY AND CONCLUSIONS

Consideration has been given to the basic design features of an electron source suited for a rocket-borne EBIL experiment utilizing an echelle spectrometer with specified fore-optics. It is concluded that a modified-Pierce design is potentially the most suitable for the application. A preliminary electron gun design is proposed which should yield a 3kV beam at a current level  $> 200$  mA. The beam geometry is poorly defined in the preliminary design, but it should be possible to obtain an acceptable beam geometry by empirical shaping of the beam-forming electrodes. A final decision on the most desirable beam geometry must await a more complete definition of the optical collection characteristics of the echelle spectrometer and the performance characteristics of the ACS.

#### REFERENCES

- Brewer, G.R., *Focusing of Charged Particles*, A. Septier (Ed.), Academic Press, New York; pp. 23-72 (1967).
- Borst, W.L., and E.C. Zipf, *Phys. Rev. A*, 1:834 (1970).
- Hansen, D.F., and M.P. Shuler, "Rocket-borne echelle spectrometer, R & D design evaluation report (U)", H.S.S., Inc., Bedford, Mass., HSS-B-029 (30 November 1976).
- Langmuir, I., and K. Blodget, *Phys. Rev.* 24:49 (1924).
- Pendleton, W.R., Jr. and L.D. Weaver, submitted.
- Pierce, J.R., *J. Appl. Phys.*, 11:548 (1940).
- Pierce, J.R., "Theory and Design of Electron Beams", Van Nostrand, Princeton, N.J. (1949).
- Spangenberg, K.R., "Vacuum Tubes", McGraw-Hill, New York (1948).

## ATTACHMENT A

AFGL DESCRIPTION/SPECIFICATIONS  
PERTINENT TO THE R & D SERVICES  
COVERED IN THE PRESENT REPORT

Line Item 0001 - Perform necessary research to design, fabricate, test and integrate a rocketborne electron beam source with the following specifications:

Subline-Line Item 0001AA - Study various electron beam source design options to maximize the photon emission rate of electron induced atmospheric radiations as viewed by a rocket based f/2 echelle spectrometer. Design tradeoffs include electron beam energy, current and cathode anode configuration. Major considerations are:

1. Maximize the f/2 spectrometer optical throughput.
2. The electron source operating altitude extends from 100 to 200 km.
3. The minimal effective photon emission rate within 1 meter distance near the payload is equivalent to or greater than that produced by a 3 kV, 50 mA electron beam.
4. The electron beam must be capable of beam shut off for several seconds three times during the course of the six minute experiment.
5. The electron beam energy and current must be constant within plus or minus ten percent of the normal operating parameters during the experiment.

## APPENDIX B

Table B1. Objective Specifications of the Rocketborne Echelle Spectrometer\*

CONFIGURATION	Littrow
ENTRANCE SLIT:	0.050 mm x 2.0 mm.
CAMERA LENS:	85 mm focal length f/2 focal ratio
INTERNAL MAGNIFICATION:	Unity
DETECTOR:	128 element self-scanning silicon photodiode array mated with channel plate multiplier image intensifier
ELEMENT SIZE:	0.05 mm x 0.43 mm
DETECTOR LENGTH:	6.5 mm (in spectral direction)
DISPERSION ELEMENT:	73 grooves/mm reflection echelle grating operating in 43rd, 55th, and 57th orders.
ORDER SORTING FILTERS:	4-cavity multilayer interference
SPECTRAL CHARACTERISTICS:	

Order	Central Wavelength	Reciprocal Dispersion	Wavelength Coverage	Wavelength Resolution
43	5627.0 $\text{\AA}$	14.9 $\text{\AA}/\text{mm}$	97 $\text{\AA}$	0.75 $\text{\AA}$
55	4399.4	11.6	76	0.58
57	4245.0	11.2	73	0.56

\*From: *Rocketborne Echelle Spectrometer*, D.F. Hansen, M.P. Shuler, Jr., and A.H. Tuttle. Final Report submitted to Air Force Geophysics Laboratories (OPR) by H.S.S., Inc., Bedford, Massachusetts under Contract F19628-76-C-0199, 1 September 1978 (HSS-B-045).

DATE  
FILMED  
— 8